

# X-ray Studies of Interfacial Strontium–Extractant Complexes in a Model Solvent Extraction System

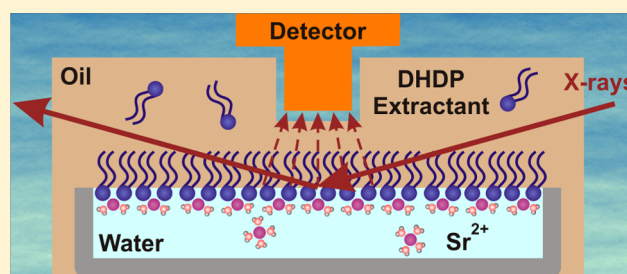
Wei Bu,<sup>\*,†</sup> Miroslav Mihaylov,<sup>†</sup> Daniel Amoanu,<sup>‡</sup> Binhua Lin,<sup>§</sup> Mati Meron,<sup>§</sup> Ivan Kuzmenko,<sup>||</sup> L. Soderholm,<sup>\*,⊥</sup> and Mark L. Schlossman<sup>\*,†</sup>

<sup>†</sup>Department of Physics and <sup>‡</sup>Department of Chemical Engineering, University of Illinois at Chicago, Chicago, Illinois 60607, United States

<sup>§</sup>Center for Advanced Radiation Sources, University of Chicago, Chicago, Illinois 60637, United States

<sup>||</sup>XSD, Advanced Photon Source and <sup>⊥</sup>Chemical Sciences and Engineering Division, Argonne National Laboratory, Argonne National Laboratory, Argonne, Illinois 60439, United States

**ABSTRACT:** The interfacial behavior of a model solvent extraction liquid–liquid system, consisting of solutions of dihexadecyl phosphate (DHDP) in dodecane and  $\text{SrCl}_2$  in water, was studied to determine the structure of the interfacial ion–extractant complex and its variation with pH. Previous experiments on a similar extraction system with  $\text{ErCl}_3$  demonstrated that the kinetics of the extraction process could be greatly retarded by cooling through an adsorption transition, thus providing a method to immobilize ion–extractant complexes at the interface and further characterize them with X-ray interface-sensitive techniques. Here, we use this same method to study the  $\text{SrCl}_2$  system. X-ray reflectivity and fluorescence near total reflection measured the molecular-scale interfacial structure above and below the adsorption transition for a range of pH. Below the transition, DHDP molecules form a homogeneous monolayer at the interface with  $\text{Sr}^{2+}$  coverage increasing from zero to saturation (one  $\text{Sr}^{2+}$  per two DHDP) within a narrow range of pH. Experimental values of  $\text{Sr}^{2+}$  interfacial density determined from fluorescence measurements are larger than those from reflectivity measurements. Although both techniques probe  $\text{Sr}^{2+}$  bound to DHDP, only the fluorescence provides adequate sensitivity to  $\text{Sr}^{2+}$  in the diffuse double layer. A Stern equation determines the  $\text{Sr}^{2+}$  binding constant from the reflectivity measurements and the additional  $\text{Sr}^{2+}$  measured in the diffuse double layer is accounted for by Gouy–Chapman theory. Above the transition temperature, a dilute concentration of DHDP– $\text{Sr}$  complexes resides at the interface, even for temperatures far above the transition. A comparison is made of the structure of the interfacial ion–extractant complex for this divalent metal ion to recent results on trivalent  $\text{Er}^{3+}$  metal ions, which provides insight into the role of metal ion charge on the structure of interfacial ion–extractant complexes, as well as implications for extraction of these two differently charged ions.



## INTRODUCTION

Solvent extraction of metal ions at the liquid–liquid interface is a chemical technique used to separate a target ion from a complex aqueous multicomponent mixture. Applications include the extraction of toxic or radioactive metals from polluted environments and nuclear waste, as well as the hydrometallurgical production of precious metals including rare earth elements.<sup>1,2</sup> The process of metal extraction often involves the transport of metal ions from the aqueous into an organic phase with the assistance of organic-soluble extractant molecules as the solubilizing agent.<sup>3,4</sup> Recent evidence suggests that efficient metal extraction may involve the self-assembly of extractants into reverse micelles in the organic phase, which enclose and shield the charge of the metal ion from the low permittivity surroundings.<sup>5,6</sup> Although it is believed that the binding and extraction of metal ions take place at the interface between aqueous and organic phases, the structural and dynamical role of the interface in this process is essentially unknown. The paucity of experimental data in this area is a

consequence of the experimental difficulties in characterizing a buried liquid–liquid interface on the appropriate temporal and spatial length scales.

As part of an ongoing project to investigate the solvent extraction of metal ions, we have utilized interface-sensitive X-ray reflectivity and fluorescence near total reflection (XFNTR) to study a model system for the solvent extraction of rare earth  $\text{Er}^{3+}$  ions. Initial experiments demonstrated the propensity for hydrated  $\text{Er}^{3+}$  ions to be located near the water surface, thus making them readily available for extraction.<sup>7</sup> Of relevance to the present study of a divalent ion,  $\text{Sr}^{2+}$ , computer simulations and nonlinear optical studies have suggested a similar, though weaker, surface activity for  $\text{Mg}^{2+}$ .<sup>8</sup> Subsequent experiments probed the liquid–liquid interface between dodecane solutions of dihexadecyl phosphate (DHDP) and aqueous solutions of

Received: August 20, 2014

Revised: September 26, 2014

Published: September 29, 2014

$\text{ErCl}_3$ , in which DHDP is the extractant and  $\text{Er}^{3+}$  is the target ion.<sup>9</sup> These experiments introduced a method to investigate the structure of interfacial ion–extractant complexes by immobilizing them at the interface as the result of thermodynamically arresting the extraction process. By use of this method, we were able to overcome the difficulties involved in using time-consuming X-ray methods to determine the structure of an otherwise short-lived interfacial intermediate in the extraction process. These measurements discovered and characterized an interfacial inverted bilayer composed of supramolecular ion–extractant complexes at the interface. The complexes contained three DHDP molecules for each  $\text{Er}^{3+}$  ion, along with a few water molecules, thus leading to charge neutrality in the vicinity of each  $\text{Er}^{3+}$ . Upon restarting the extraction process,  $\text{Er}^{3+}$  was transferred to the dodecane in the form of a supramolecular Er–extractant complex. X-ray absorption fine structure (XAFS) measurements of the extracted Er–DHDP complex in solution demonstrated that its atomic coordination was consistent with the structure of Er–DHDP complexes at the interface.<sup>9</sup> These measurements suggested a causal connection between ion–extractant complexes formed at the interface and those extracted into the bulk oil. Therefore, the interfacial Er–DHDP ion–extractant complex is an intermediate state in the extraction process as the ion passes from its hydrated state in the aqueous phase through the interface to form reverse micelles in the organic phase.

The inverted bilayer observed in the Er–DHDP system presents a counterintuitive interfacial structure, in which DHDP head groups are separated from the water surface and DHDP tail groups in the lower leaflet of the bilayer are in contact with it.<sup>9</sup> This structure has been rationalized by considering that Er ions at the water surface, upon complexation with DHDP molecules approaching from the oil side of the interface, undergo a dynamic interfacial instability that drags them out of the water to form an ion–extractant complex at the interface. The previously mentioned experiments were designed to trap ion–extractant complexes at the interface in the midst of this dynamical process. Nevertheless, the long-term stability of the inverted bilayer at the interface allowed it to be studied for more than a day.<sup>9</sup> It has been hypothesized that the stability of an inverted bilayer structure is dominated by the favorable electrostatic interactions of the three DHDP head groups with  $\text{Er}^{3+}$ , which are optimized in the inverted bilayer phase over the configuration that can be achieved when three DHDP molecules on the oil side of the interface try to interact with an aqueous  $\text{Er}^{3+}$  ion. Presumably, the inverted bilayer will not form if the electrostatic attraction of the metal ion is too weak or if the DHDP molecules required for a neutral complex can interact easily with a metal ion while staying on the opposite side of the oil–water interface. The current experiments on  $\text{Sr}^{2+}$  were designed to test this idea.

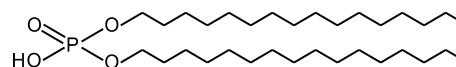
It is well-known that pH and the valence of the metal ion plays a critical role in determining the efficiency of metal extraction;<sup>10</sup> therefore, it is sensible to hypothesize that they influence the formation of metal–extractant complexes at the interface. To explore the role of the charge of the target metal ion and the influence of pH on the interfacial structure, we extend our previous studies by utilizing surface X-ray reflectivity and fluorescence techniques to investigate the structure of the oil–water interface between dodecane solutions of DHDP and aqueous solutions of  $\text{SrCl}_2$ . Varying the pH value of the aqueous solution yields measurements of the ion-binding properties of phosphate head groups. In addition to its

implications for solvent extraction, the current work also provides quantitative studies on ion–lipid binding that may have some relevance for biological membranes and the formation of Langmuir–Blodgett multilayers.

## EXPERIMENTAL SECTION

**Materials.** The dodecane–water interface was selected for this study because of its wide use in industrial applications of solvent extraction. Dodecane ( $\text{CH}_3(\text{CH}_2)_{10}\text{CH}_3$ , >99%, Sigma-Aldrich) was purified by passing it six times through activated alumina in a chromatography column<sup>11</sup> and filtering it through a 0.2  $\mu\text{m}$  Omnipore membrane paper to remove surface active impurities. The extractant, dihexadecyl phosphate (DHDP,  $[\text{CH}_3(\text{CH}_2)_{15}\text{O}]_2\text{POOH}$ , >98%, Sigma-Aldrich; Chart 1), was

Chart 1. Di-hexadecyl Phosphate (DHDP)



purified by recrystallizing it twice from chloroform.<sup>12</sup> The  $10^{-4}$  M DHDP dodecane solution was prepared at 50 °C due to its low solubility at room temperature, and then cooled to the desired temperature. In the experiments the concentration of DHDP solutions was always below the solubility limit.

Strontium chloride ( $\text{SrCl}_2$ , >99.99%, Alfa Aesar) was roasted at 500 °C for 30 min to remove organic impurities. Hydrochloric acid (HCl Optima\*, Fisher Scientific), acetate buffer (acetic acid, >99.9985% and sodium acetate, >99.9985%, Alfa Aesar), and phosphate buffer (sodium phosphate monobasic, >99.999% and sodium phosphate dibasic, >99.999%, Sigma-Aldrich) were used without further purification to adjust the pH values of  $\text{SrCl}_2$  solutions over the pH range <4, 4–5.7, and >5.7, respectively. The Henderson–Hasselbalch equation provides a convenient way to calculate pH:  $\text{pH} = \text{p}K_a + \log [A^-]/[HA]$ , where  $[HA]$  and  $[A^-]$  are the concentrations of weak acid and its conjugate base.  $\text{p}K_a = -\log K_a$  (4.76 and 7.2 for the acetate and phosphate buffer, respectively), where  $K_a$  is the acid dissociation constant. The buffer concentration (i.e.,  $[A^-] + [HA]$ ) is kept at 2 mM for all  $\text{SrCl}_2$  solutions. A pH meter was used to measure the pH for all aqueous solutions. Differences between the measured and calculated values, which could be as large as  $\Delta\text{pH} = 0.25$  for the acetate buffer, but less than 0.1 for the two other buffers, were attributed to sample preparation and the accuracy of the pH meter (HANNA; Model PH212). The choice of strontium concentration, typically  $10^{-5}$  M, was chosen to meet the following criteria: the extractant concentration is usually 10 times greater than the salt in real solvent extraction systems and the DHDP extractant concentration should be small enough to eliminate the possibility of interfacial precipitation. Strontium retains  $\text{Sr}^{2+}$  speciation within the aqueous phase and experimental pH range (3.2–6.2).<sup>13</sup> Strontium does not partition into the dodecane to any appreciable extent. Ultrapure water from a Nanopure UV Barnstead system was used to prepare all aqueous solutions.

**Interfacial Tension Measurements.** Interfacial tensions were measured with a Wilhelmy plate made of chromatography paper that passes fully into the upper organic phase to make contact with the aqueous–organic interface. This plate is fully wet by the aqueous solution. The plate is hung on a platinum wire from a Cahn microbalance, which measures the force on the plate. A reference force was measured with the plate

suspended just above the interface, and then the bottom edge of the plate was lowered into contact with the interface and the force remeasured. The interfacial tension is the difference between these two measurements divided by the wetted perimeter of the Wilhelmy plate.<sup>14</sup> Samples were contained in a glass dish surrounded by a custom-designed thermostat that controls the temperature to  $\pm 0.005$  °C. Interfacial tension measurements were measured as a function of temperature for a series of values of pH.<sup>15,16</sup> The pH, which was recorded throughout the temperature range of interfacial tension measurements, did not depend on temperature. Samples were kept at high temperature for approximately 2 h, and then interfacial tensions were recorded during the following cooling process. Occasional samples were measured during subsequent reheating, with excellent reproducibility. Prior to each measurement of interfacial tension, approximately 1.5–2 h are required before equilibrium conditions are reached, as defined by variations of temperature and interfacial tension smaller than 0.01 °C and 0.03 mN/m over a 10 min interval.

The interfacial tension measurements were also used to examine the purity of the solvent and surfactant. The interfacial tension of the pure dodecane/pure water interface was measured to be  $51.8 \pm 0.3$  mN/m at 22 °C, in good agreement with literature values.<sup>17–19</sup> The interfacial tension was stable (varying within the error bar) for many hours immediately after the formation of the interface, confirming that the solvents were free of surface-active impurities.<sup>11</sup> With the presence of  $10^{-4}$  M DHDP in the organic phase, the interfacial tension exhibited a negligible hysteresis ( $<0.1$  °C) in an adsorption transition temperature upon heating or cooling through the transition, indicating that the purity of both solvent and surfactant is adequate.<sup>15</sup>

**Liquid–liquid Sample Cell.** X-ray surface scattering requires a flat interface because the angles of scattering are very small (down to  $\sim 5 \times 10^{-4}$  rad).<sup>20</sup> Although a liquid interface can be flattened by increasing its dimension along the X-ray path, the resultant long X-ray path through the upper liquid phase will lead to large X-ray absorption and excessive background scattering. To balance these competing effects, a customized liquid–liquid sample cell for X-ray scattering measurements was designed to reduce the interfacial curvature (Figure 1).

The mainframe of the cell is made of Teflon-coated aluminum, which has good thermal conductivity. The aqueous phase is in a glass tray surrounded by dodecane. The glass tray is cleaned in a sulfuric acid solution of ammonium persulfate (18 g/L) to render it hydrophilic. However, the rim of the glass tray is rendered effectively hydrophobic by roughening it with a grinder during the manufacturing process and then wetting it by drops of dodecane prior to filling the tray with water. The inside edge of the rim pins the dodecane–water interface. Adjusting the volume of the aqueous solution with a syringe and leveling the sample cell along the axes parallel and perpendicular to the incident X-ray beam produces a flat interface with a typical radius of curvature of a few hundred meters. When the sample interface is sufficiently flat, the X-ray reflectivity is constant as an X-ray beam is scanned across the interface at a fixed angle of incidence. The interfacial area, determined by the glass tray dimension, is  $80 \times 60$  mm<sup>2</sup> (along the beam  $\times$  transverse).

A Vortex-60EX multicathode energy dispersive X-ray detector (SII Nano Technology USA, Inc.) is placed in a cylindrical well above the interface. It collects fluorescent X-rays

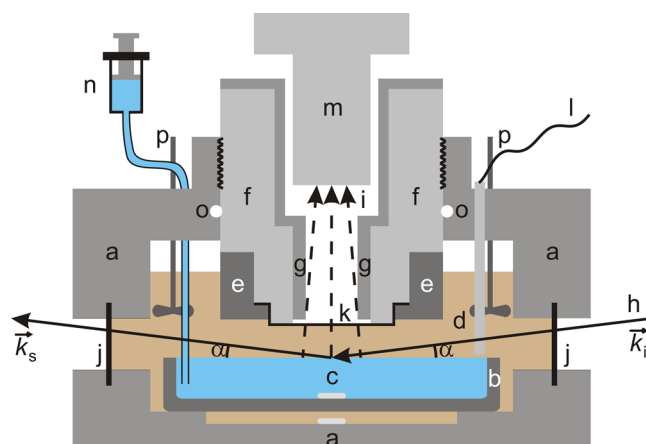


**Figure 1.** Cross-sectional view of the sample cell. Main components of the cell are indicated as (a) Teflon coated aluminum mainframe, (b) glass tray, (c) aqueous phase, (d) organic phase, (e) stainless steel cap, (f) detector well, (g) Teflon collimator, (h) X-ray beam:  $k_i$ , incident X-ray wave vector;  $k_s$ , scattered or reflected wave vector, and angles of incidence and reflection,  $\alpha$ , (i) fluorescent X-ray beams from the sample, (j) Mylar windows (150  $\mu$ m thick), (k) Kapton window (7  $\mu$ m thick), (l) platinum resistance temperature probe (Omega PT 100), (m) Vortex-60EX energy dispersive detector with 60 mm snout, (n) syringe, (o) Teflon O-ring, and (p) Teflon propellers. Two Teflon coated stir bars are placed in and below the glass tray.

from the sample (indicated schematically by dashed lines in Figure 1). Atomic fluorescence from the interface must pass through a thin layer of dodecane between the interface and a Kapton window that caps the bottom of the cylindrical well. The distance between the bottom of the well and the interface can be adjusted to reduce the thickness of the dodecane layer to  $\sim 0.5$  mm, without altering the interfacial shape, to minimize absorption of fluorescent X-rays by dodecane. A 0.5 mm thick layer is much thinner than the 18.14 mm attenuation length in dodecane of the Sr  $K\alpha$  emission line at 14.148 keV. Less than 3% of the fluorescence intensity is absorbed upon passing through the dodecane. A cylindrical Teflon collimator (6.1 mm inside radius and 25.4 mm in length) defines the detection volume, i.e., the projection of the active area of the detector (4 mm radius) onto the sample, whose cross-section is a circle with a radius of 6.5 mm at the position of the liquid–liquid interface. The fluorescence intensity from  $\text{Sr}^{2+}$  is produced within the overlap region of this detection volume and the incident X-ray path, as discussed in detail later.

Mylar and Kapton films, both X-ray transparent materials, were used as X-ray windows for the incident and reflected beam and to cap the bottom of the fluorescence detector well. The three windows are sealed leak-tight with Teflon-coated O-rings. A platinum temperature probe (OMEGA) encased in a Teflon sheath is placed just above the dodecane–water interface to record the sample temperature. Two Teflon propellers in the dodecane and two Teflon-coated stir bars in and below the glass tray stir both phases during each temperature change, allowing the sample to reach thermal equilibrium quickly. For precise temperature control ( $\pm 0.01$  °C), the sample cell is contained in a thermostat similar to the one used for interfacial tension measurements. The thermostat has X-ray windows made from Kapton films and a Lakeshore 340 controls its temperature.

**Liquid Surface Reflectometer.** X-ray measurements were carried out on beamlines 9-ID and 15-ID at the Advanced



Photon Source (Argonne National Laboratory) with an X-ray energy of 22.117 keV (wavelength  $\lambda = 0.56058 \text{ \AA}$ ) at 9-ID and 20 keV ( $\lambda = 0.61992 \text{ \AA}$ ) at 15-ID. We used a liquid surface reflectometer, described in detail elsewhere,<sup>21,22</sup> for both X-ray reflectivity and X-ray fluorescence near total reflection measurements. A schematic of the instrument at 15-ID is shown in Figure 2. A monochromatic X-ray beam is deflected

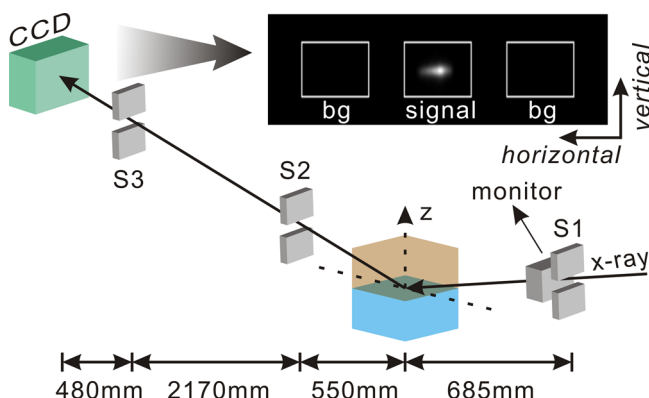


**Figure 2.** Sketch of the surface scattering setup at 15-ID for X-ray reflectivity measurements. Slits S1 and S2 are positioned before and after the sample. The monitor is an ionization chamber filled with helium gas to monitor the incident beam intensity. An area detector CCD (Burker APEXII) and its front slit (S3) are far from the sample ( $\sim 3.2 \text{ m}$  from sample center to CCD face) for increased angular resolution. A characteristic image of the CCD detector is displayed, where “bg” refers to the background measured away from the specular reflection signal.

to a desired angle of incidence by a crystal monochromator. It passes through the upper organic phase to reflect off the dodecane–water interface. An ionization chamber (“monitor” in Figure 2) monitors the variation of incident beam intensity, while the outgoing beam intensities, including the reflected and fluorescent beams, are recorded by specialized detectors (i.e., CCD area detector at 15-ID, Mythen linear detector at 9-ID, and Vortex-60EX at both beamlines). A set of absorbers (not shown in Figure 2) is inserted between the sample and the monitor to reduce the incident beam intensity to an optimal level, which is low enough to avoid saturating the detector, as well as eliminate or reduce radiation damage to the sample below a detectable level. The size of the incident beam is set by a  $15 \mu\text{m} \times 1 \text{ mm}$  (height  $\times$  width) slit (“S1” in Figure 2) located before the ionization chamber,  $\sim 685 \text{ mm}$  from the sample center. The small beam height ensures that the incident beam footprint on the interface is smaller than the flat region of the interface at all incident angles used for reflectivity measurements, but larger than the  $13 \text{ mm}$  length of the fluorescence detection volume (projected onto the interface) for the small incident angles used for fluorescence measurements.

**X-ray Reflectivity.** Synchrotron X-ray surface scattering techniques, such as X-ray reflectivity and off-specular diffuse scattering, among others, have been used to determine the molecular-scale structure of liquid–liquid interfaces, including surfactant monolayers<sup>15,23–25</sup> and ionic distributions<sup>26–30</sup> with subnanometer spatial resolution. X-ray reflectivity, whose kinematics is illustrated in Figure 1, probes the electron density variation  $\rho(z)$  along the direction  $z$  perpendicular to the interface, but averaged over the  $x$ - $y$  region of the X-ray footprint on the interface. Reflectivity data are measured as a

function of the wave vector transfer,  $Q_z = |\vec{k}_s - \vec{k}_i| = 2k_0 \sin \alpha$ , where  $k_0 = 2\pi/\lambda$  is the wavenumber,  $\vec{k}_i$  is the incident wave vector, and  $\vec{k}_s$  is the scattered or reflected wave vector. As illustrated in Figure 2, reflectivity data at each  $Q_z$  consists of measurements of the specularly reflected X-ray intensity (at  $Q_{xy} = 0$ ), and the background intensity measured slightly off from the specular condition (i.e.,  $Q_{xy} \neq 0$  but small). Both intensities are normalized to the incident beam intensity prior to further analysis.

X-ray reflectivity data at 15-ID were measured with a Bruker Apex II CCD area detector shown in Figure 2, which simultaneously measures the signal and background, shortening the measurement time significantly. The detector resolution is achieved by grouping a  $4 \times 4$  set of pixels into one virtual pixel of dimension  $60 \times 60 \mu\text{m}^2$ . A fraction of the direct beam penetrates through the aqueous phase and the glass tray after transmitting through the interface, and eventually strikes the CCD detector. This direct beam can be separated from the reflected beam signal on the CCD even at the smallest angles used for reflectivity measurements ( $5 \times 10^{-4} \text{ rad}$ ). A vertical slit of  $1 \text{ mm}$  gap (S2 in Figure 2) is placed between the sample and the CCD detector at a distance of  $\sim 550 \text{ mm}$  from the sample to reduce bulk scattering. This slit is mounted on an arm that follows the reflected beam to ensure that it passes through the center of the slit as  $Q_z$  varies.<sup>22</sup> The CCD detector is fixed in position, though it has a large enough active area ( $\sim 6 \times 6 \text{ cm}^2$ ) to detect the reflected beam throughout the entire range of  $Q_z$  used for reflectivity measurements. A  $5 \text{ mm}$  vertical slit (S3 in Figure 2) is placed  $\sim 480 \text{ mm}$  in front of the CCD detector to reduce background scattering from the experimental hutch. Although the slit is mounted in a fixed position, its jaws are moved to follow the reflected beam. The lower jaw is set to block the direct beam. A characteristic CCD image, displaying a reflection signal, is shown in Figure 2. The reflected beam intensity is calculated by summing over a region of  $30 \times 60$  (height  $\times$  width) virtual pixels ( $1.8 \times 3.6 \text{ mm}^2$ ; see white frame in Figure 2), whose center is determined by a 2-dimensional Gaussian function fit to the signal. The background is defined as the average integrated intensity over two similar regions displaced  $0.1^\circ$  horizontally to both sides, as shown in Figure 2. The characteristic image shown in Figure 2 is only a small fraction ( $<2\%$ ) of the entire CCD image. Reflection measurements at 9-ID were taken with a similar setup, although the data were collected by a Mythen linear detector, which is mounted on the reflectometer much closer to the sample ( $\sim 900 \text{ mm}$ ).

The electron density profile  $\rho(z)$  is determined by fitting X-ray reflectivity data to a model constructed from a sum of error functions,<sup>22,31</sup>

$$\rho(z) = \frac{1}{2} \sum_{i=0}^{N-1} \text{erf}\left(\frac{z - z_i}{\sqrt{2}\sigma}\right) (\rho_i - \rho_{i+1}) + \frac{\rho_0 + \rho_N}{2} \quad (1)$$

where  $\text{erf}(z) = (2/\sqrt{\pi}) \int_0^z e^{-t^2} dt$ ,  $N$  is the number of internal interfaces,  $\rho_i$  is the electron density of slab  $i$  with  $\rho_0 = \rho_{\text{aq}}$  and  $\rho_N = \rho_{\text{oil}}$  (i.e., the electron densities of the bulk aqueous and dodecane phases),  $z_i$  is the position of interface  $i$ , and  $\sigma$  is the interfacial roughness. The thickness of slab  $i$ ,  $d_i$ , is defined as  $|z_i - z_{i-1}|$ . X-ray reflectivity is calculated from the Parratt formalism by discretizing the density profile in eq 1.<sup>32</sup> Nonlinear least-squares fitting is used to determine the minimum number,  $N - 1$ , of internal slabs required to fit the X-ray reflectivity data, where the minimum number of internal

slabs is defined by that number for which an additional slab does not improve the quality of the fit substantially. Fitting variables that number  $2N - 1$  include  $\rho_i$  and  $d_i$  for each internal slab and  $\sigma$ . The interfacial roughness  $\sigma$  is calculated from capillary wave theory for the purpose of comparing it to the fitted values, using<sup>22</sup>

$$\sigma^2 = \frac{k_B T}{2\pi\gamma} \ln \frac{4}{Q_z \Delta\beta r_A} \quad (2)$$

where  $k_B$  is the Boltzmann constant,  $T$  is the temperature in Kelvin,  $\gamma$  is the interfacial tension,  $\Delta\beta$  is the angular acceptance of the detector (0.58 and 0.67 mrad for 15-ID and 9-ID, respectively), and  $r_A$  is the average radius of the relevant atom or molecule at the interface.

**X-ray Fluorescence Near Total Reflection (XFNTR).** XFNTR, first introduced by Bloch et al.,<sup>33</sup> has been widely used to detect the existence and coverage of metal ions at liquid–vapor<sup>34–37</sup> and liquid–liquid interfaces,<sup>9,38</sup> by taking advantage of its high elemental selectivity. XFNTR data consists of measurements of fluorescence spectra from the sample at a series of  $Q_z$  near total reflection. The critical wave vector transfer for total reflection  $Q_c = 4[\pi r_e(\rho_{\text{aq}} - \rho_{\text{oil}})]^{1/2}$ , where  $r_e = 2.818$  fm is the classical electron radius, has the value  $Q_c = 0.01035 \text{ \AA}^{-1}$  for the interface between  $10^{-4}$  M DHDP in dodecane and  $10^{-5}$  M  $\text{SrCl}_2$  in water at  $28^\circ\text{C}$ . Slight variations of  $Q_c$  with temperature are taken into account in modeling the data. XFNTR signals below and above  $Q_c$  are dominated by the interface and the bulk, respectively, because the X-ray penetration depth changes quickly near the critical angle: from nanometers for  $Q_z < Q_c$  to micrometers for  $Q_z > Q_c$ . Here, we review and introduce details of the XFNTR technique that are important for its application to liquid–liquid interfaces.

Calculation of the fluorescence intensity requires consideration of the scattering geometry shown in Figure 3, which

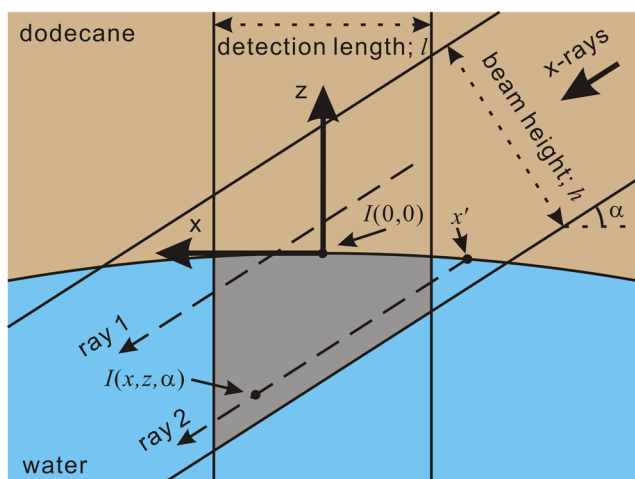


**Figure 3.** Schematic diagram for the calculation of the fluorescence intensity. The X-ray incident angle and the interfacial curvature are exaggerated for clarity.

illustrates a convex dodecane–water interface with a radius of curvature  $R_C$ , where we assume that  $R_C$  is constant across the interface. The relative correction of the incidence angle  $\Delta\alpha/\alpha$  due to transverse curvature in the other direction, in the  $y$ – $z$  plane,  $\Delta\alpha/\alpha = 1 - \cos(|y|/R_C)$ , is negligible because the transverse beam footprint ( $|y| \sim 0.5$  mm) is significantly smaller than  $R_C$  ( $\sim 200$  m). The central ray of an X-ray beam of height

$h$  strikes the interface with incident angle  $\alpha$  at the sample center. The cross-section of the overlap of the X-ray beam with the detection volume of the fluorescence detector is sketched in Figure 3. The fluorescence intensity is calculated by integrating the X-ray intensity and the  $\text{Sr}^{2+}$  concentration over the overlap region in the aqueous phase (shown in gray in Figure 3). The footprint of the incident beam, defined as  $h/\alpha$  for small  $\alpha$ , is larger than the detection length  $l$  ( $=13$  mm) for all values of  $Q_z$  measured, making a footprint correction unnecessary for the data analysis.

Figure 3 illustrates two rays within the X-ray beam that strike the interface at different positions and, consequently, have different incident angles because the interface is not flat. In this analysis, we assume that rays within the X-ray beam are all parallel. This can be justified by noting that the vertical divergence at the Advanced Photon Source is an order of magnitude smaller than the effects of sample curvature in the  $x$ – $z$  plane. The angle of incidence at position  $x'$  for ray 2 that passes through position  $(x, z)$  is given by  $\alpha' \approx \alpha - x'/R_C$  for large  $R_C$  ( $\gg h/\alpha$ ), where  $x' \approx x + z/\alpha$ . If the intensity at the center of the interface,  $I(0,0)$ , is normalized to unity, then the intensity of the X-ray beam in the aqueous phase,  $I(x,z,\alpha)$ , is given by

$$\frac{I(x,z,\alpha)}{I(0,0)} = T(\alpha') e^{-|z|/\Lambda(\alpha')} e^{-\mu_0 x'} \quad (3)$$

where  $\mu_0$  is the absorption coefficient of the incident beam in the organic phase ( $0.21$  and  $0.24 \text{ cm}^{-1}$  for X-ray energies of  $20.000$  and  $22.117$  keV, respectively),<sup>39</sup> and  $T(\alpha') = [2\alpha'/(\alpha' + (\alpha'^2 - \alpha_c^2)^{1/2})]^2$  is the Fresnel transmission with a maximum value of  $4$  at  $\alpha' = \alpha_c$  (where  $\alpha_c = Q_c/2k_0$  is the critical angle). The penetration depth in the aqueous phase  $\Lambda(\alpha') = 1/[2k_0 \text{Im}((\alpha'^2 - \alpha_c^2 + 2i\beta)^{1/2})]$  (where  $\beta$  is the imaginary part of the refractive index of the aqueous phase) varies from  $\sim 100 \text{ \AA}$  well below the critical angle  $\alpha_c$  to a maximum of several  $\mu\text{m}$  above  $\alpha_c$  in the experimental range of  $Q_z$ . Equation 3 is a good approximation under the assumption that variations of the  $\text{Sr}^{2+}$  concentration near the interface are weak and occur within a depth smaller than  $\Lambda(\alpha')$ . The exponential factors on the right side of eq 3 account for X-ray absorption in the aqueous and organic phases. One should note that the penetration depth  $\Lambda(\alpha')$  also varies with bulk salt concentration and X-ray beam energy. The emission line intensity from one  $\text{Sr}^{2+}$  ion at the position  $(x, z)$  is proportional to  $I(x,z,\alpha) e^{-\mu_{\text{Sr}}(E)|z|}$ , where the energy dependent  $\mu_{\text{Sr}}(E)$  is the absorption coefficient of the Sr emission line of energy  $E$  in the aqueous phase ( $\mu_{\text{Sr}}(E) = 1.78 \text{ cm}^{-1}$  for  $K\alpha$  line).<sup>39</sup>

Assuming that the  $\text{Sr}^{2+}$  concentration is uniform everywhere in the aqueous phase except in the interfacial region ( $0 < |z| \ll \Lambda(\alpha')$ ), the total fluorescence intensity is the sum of the interfacial  $I_{\text{int}}$ , bulk  $I_{\text{bulk}}$ , and background  $I_{\text{bg}}$  contributions, given by

$$\begin{aligned} I/I_0 &= (I_{\text{int}} + I_{\text{bulk}} + I_{\text{bg}})/I_0 \\ &= \frac{C}{A_{\text{Sr}}} \int T(\alpha') e^{-\mu_0 x'} dx' \\ &\quad + C n_{\text{Sr}} \iint T(\alpha') e^{-|z|/\Lambda(\alpha',E)} e^{-\mu_0 x'} dx dz + I_{\text{bg}}/I_0 \end{aligned} \quad (4)$$

where  $I_0$  is the incident beam intensity and  $C$  is a scale factor for a given emission line that accounts for the effect of the

scattering geometry. This factor has units of length ( $\text{\AA}$ ) because it includes the integration along the  $y$ -direction, which is constant for fixed incident beam width. The interfacial area per  $\text{Sr}^{2+}$  ion is given by  $A_{\text{Sr}}$ , the bulk number density of  $\text{Sr}^{2+}$  ions is given by  $n_{\text{Sr}}$ , and  $\Lambda(\alpha', E) = \Lambda(\alpha') / (\Lambda(\alpha')\mu_{\text{Sr}}(E) + 1)$  ( $\approx \Lambda(\alpha')$ ) because  $\Lambda(\alpha')\mu_{\text{Sr}}(E) \ll 1$  is the effective penetration depth of the incident beam in the aqueous phase that accounts for X-ray absorption of the incident and fluorescent beams. The first term in eq 4 represents the intensity from excess ions at the interface. Because the thickness of the interfacial region is small ( $\ll \Lambda(\alpha')$ ), the exponential decay in  $z$  vanishes from the integration, which can be numerically solved in the range  $x' \in [-1/2, 1/2]$ . If the interface is flat, the interfacial intensity can be simplified as  $I_{\text{int}}/I_0 = 2CT(\alpha) \sinh(\mu_0 l/2) / A_{\text{Sr}}\mu_0$  ( $\approx CT(\alpha)l/A_{\text{Sr}}$  for  $\mu_0 l \ll 1$ ). The bulk intensity, expressed as the second term in eq 4, is essentially the product of  $Cn_{\text{Sr}}$  and the integration of the X-ray intensity over the gray area in Figure 3.

The background intensity  $I_{\text{bg}}$  is the result of a secondary scattering process in which the incident beam is scattered first from dodecane in the organic phase and then penetrates into the lower aqueous phase to produce additional fluorescence from ions in that phase. Although the background intensity  $I_{\text{bg}}$  cannot be measured directly, it can be measured to a good approximation by an X-ray beam transmitted through the top (dodecane) phase above and parallel to the interface (within  $\sim 100 \mu\text{m}$  in our measurements). This transmission mimics the X-ray beam path for a measurement at any given  $Q_z$  in the sense that secondary scattering from the transmitted X-ray beam suffers little absorption when it penetrates through the thin layer of dodecane into the aqueous phase, where it produces “background” fluorescence.

The second integration in eq 4 is complicated because  $\alpha'$  and  $x'$  have a nontrivial dependence on the  $x$ – $z$  coordinates, as shown in Figure 3. Because  $\alpha'$  and  $x'$  are fixed for a given ray, the integration can be simplified by integrating the X-ray intensity in  $z$  along the portion of each ray in the gray area to yield  $I_{\text{ray}}$ , followed by integrating  $I_{\text{ray}}$  in  $x'$  across the footprint. Single rays can be categorized according to where they strike the interface (Figure 3): left side ( $x' \in [1/2, h/2a]$ ), middle ( $x' \in [-1/2, 1/2]$ , e.g., ray 1), and right side ( $x' \in [-h/2a, -1/2]$ , e.g., ray 2). The first category contains rays that do not contribute to the fluorescence intensity, whereas  $I_{\text{ray}}$  for the other two are given by

$$\frac{I_{\text{ray}}(x')}{I_0} = \begin{cases} T(\alpha')e^{-\mu_0 x'} \tilde{\Lambda}(\alpha', E) \times (1 - e^{(x'-1/2)\alpha/\tilde{\Lambda}(\alpha', E)}) & x' \in [1/2, h/2a] \\ T(\alpha')e^{-\mu_0 x'} \tilde{\Lambda}(\alpha', E)(e^{(x'+1/2)\alpha/\tilde{\Lambda}(\alpha', E)} - e^{(x'-1/2)\alpha/\tilde{\Lambda}(\alpha', E)}) & x' \in [-h/2a, -1/2] \end{cases} \quad (5)$$

The bulk fluorescence intensity  $I_{\text{bulk}}$  is then calculated numerically by integrating over  $x'$ ,

$$I_{\text{bulk}}/I_0 = \frac{Cn_{\text{Sr}}}{I_0} \int_{-h/2a}^{1/2} I_{\text{ray}}(x') dx' \quad (6)$$

## RESULTS AND ANALYSIS

**Interfacial Tension Measurements.** Studies of nonionic single chain surfactants soluble in liquid alkanes have demonstrated the existence of an adsorption transition at which surfactants adsorb onto the liquid–liquid interface with

water.<sup>15,23,24,40,41</sup> A 2-dimensional (2D) condensed phase, either a 2D liquid or 2D solid that varies with surfactant, exists at the interface below the transition temperature. Above the phase transition the interface has been shown to contain a dilute concentration of surfactants referred to as a 2D gas. A signature of the adsorption transition is a change in slope of the temperature variation of interfacial tension  $\gamma$ , which indicates a change in the interfacial excess entropy per unit area  $S_a^\sigma = -(\text{d}\gamma/\text{d}T)_{p,c_i}$  measured at fixed pressure and composition. Note that a change in  $S_a^\sigma$  can be the result of other aspects of molecular ordering, such as chain ordering. X-ray measurements presented later indicate that both adsorption and chain ordering take place as the temperature is lowered through this transition. Figure 4 illustrates the interfacial tension as a

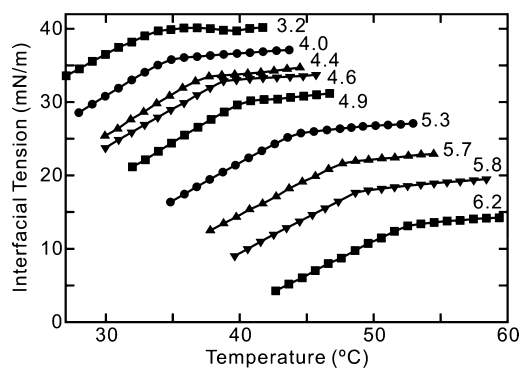


**Figure 4.** Interfacial tension as a function of temperature for the interface between  $10^{-4}$  M DHDP in dodecane and  $10^{-5}$  M  $\text{SrCl}_2$  in water with pH values indicated.

function of temperature for the interface between  $10^{-4}$  M DHDP in dodecane and  $10^{-5}$  M  $\text{SrCl}_2$  in water. A range of pH values of the aqueous solutions, varying from 3.2 to 6.2, were selected by the choice of HCl, acetate, or phosphate buffer (Table 1).

Figure 4 shows that the interfacial tension data at different pH have the same shape, in which a sharp change in slope appears. All of these curves lie below the interfacial tension for a pure dodecane–water interface, which exhibits a slightly negative slope, over this range in temperature with values of  $\gamma$  varying from 51.7 to 50.5 mN/m. The characteristic change in slope  $(\text{d}\gamma/\text{d}T)_{p,c_i}$  when DHDP is present demonstrates that DHDP molecules undergo a single transition from a low temperature ordered phase to a high temperature disordered phase at dodecane–water interfaces.<sup>15,42</sup> The transition temperatures,  $T_o$ , defined by the location of the kink in the curve, exhibit a monotonic increase with pH (Table 1). The slightly positive slope  $(\text{d}\gamma/\text{d}T)_{p,c_i}$  above the transition temperature suggests the presence of a smaller but non-negligible concentration of DHDP at the interface, as discussed later.

The interfacial excess entropy per unit area  $S_a^\sigma = -(\text{d}\gamma/\text{d}T)_{p,c_i}$  is the excess entropy of molecules at the interface over their entropy in the bulk. The change in the interfacial excess entropy across the transition  $\Delta S_a^\sigma$  is given by the difference in  $S_a^\sigma$  on either side of the transition as  $\Delta S_a^\sigma = (S_a^\sigma)_{T>T_o} - (S_a^\sigma)_{T<T_o}$  (Table 1). The average value  $\Delta S_a^\sigma = 0.86 \pm 0.1 \text{ mJ}/(\text{m}^2 \text{ K})$  is comparable to values observed for surface freezing ( $0.7 \text{ mJ}/(\text{m}^2 \text{ K})$ )<sup>43</sup> and bulk rotator–liquid phase transitions ( $0.83 \text{ mJ}/(\text{m}^2 \text{ K})$ )<sup>44</sup> in 1-hexadecanol ( $\text{CH}_3(\text{CH}_2)_{15}\text{OH}$ ), which has the same chain length as DHDP.



Table 1. Interfacial Tension Measurements and Experimental Conditions Relevant for X-ray Studies<sup>a</sup>

	pH								
	3.2	4.0	4.4	4.6	4.9	5.3	5.7	5.8	6.2
HCl (mM)	0.63								
CH <sub>3</sub> COOH (mM)		1.70	1.39	1.18	0.84	0.45	0.21		
CH <sub>3</sub> COONa (mM)		0.30	0.61	0.82	1.16	1.55	1.79		
NaH <sub>2</sub> PO <sub>4</sub> (mM)								1.84	1.63
Na <sub>2</sub> HPO <sub>4</sub> (mM)								0.16	0.37
T <sub>0</sub> (°C)	33.8 ± 1.9	34.6 ± 0.5	37.0 ± 1.0	38.7 ± 0.5	40.0 ± 0.7	44.1 ± 0.7	47.5 ± 0.9	48.9 ± 0.7	52.4 ± 1.3
ΔS <sub>α</sub> <sup>σ</sup> (mJ/(m <sup>2</sup> K))	0.93 ± 0.05	0.97 ± 0.01	0.93 ± 0.03	0.95 ± 0.01	0.93 ± 0.02	0.87 ± 0.01	0.78 ± 0.02	0.79 ± 0.01	0.78 ± 0.02
T <sub>X-ray</sub> (±0.005 °C)	28.657	28.896	31.695	30.586	32.720	36.730	38.780	41.900	44.950
γ <sub>X-ray</sub> (±2 mN/m)	35.8	29.8	27.7	25.4	22.3	18.6	13.6	11.4	6.4
σ <sub>cap</sub> (Å)	3.9	4.2	4.4	4.6	4.9	5.5	6.4	7	9.6
σ <sub>cap</sub> <sup>*</sup> (Å)	3.4	3.7	3.8	4.0	4.2	4.7	5.4	5.9	7.9

<sup>a</sup>T<sub>0</sub> is the transition temperature, ΔS<sub>α</sub><sup>σ</sup> is the change in interfacial excess entropy per unit area across the transition, and T<sub>X-ray</sub> is the experimental temperature for X-ray measurements. The listed interfacial tension γ<sub>X-ray</sub> is a value estimated using the X-ray measurement temperature T<sub>X-ray</sub> and the measured values in Figure 4, with an estimated uncertainty that includes the consequence of uncertainty in pH values among samples. Values of interfacial roughness calculated from capillary wave theory (eq 2) are provided for comparison to the fitted values described later and are calculated at the value of γ<sub>X-ray</sub> for a given pH without (σ<sub>cap</sub>) and with (σ<sub>cap</sub><sup>\*</sup>) bending rigidity set equal to 20 k<sub>B</sub>T.<sup>22</sup>

**X-ray Reflectivity.** Each sample studied with X-rays was prepared as follows. A dodecane solution of DHDP heated to a few degrees above T<sub>0</sub> was poured on top of an aqueous SrCl<sub>2</sub> solution held in a sample thermostat kept a few degrees below T<sub>0</sub>. Subsequently, the sample was equilibrated at the value of T<sub>X-ray</sub> (below T<sub>0</sub>) listed in Table 1 for approximately 2 h. As shown previously for studies of Er<sup>3+</sup> extraction using ErCl<sub>3</sub> aqueous phases,<sup>9</sup> this protocol allows for ion extraction during the time when the interface temperature is above T<sub>0</sub>, but greatly retarded, or arrested, extraction when the interface temperature drops to temperatures below T<sub>0</sub>. This thermal protocol proved useful in the earlier studies of Er<sup>3+</sup> extraction because it allowed us to immobilize ion–extractant complexes at the interface, which had formed while extraction was ongoing. The same temperature protocol was used for these experiments on SrCl<sub>2</sub> to facilitate comparison with the earlier experiments on ErCl<sub>3</sub>.<sup>9</sup> To ensure that X-rays probe the high density phase of DHDP at the dodecane–water interface, the experimental temperature T<sub>X-ray</sub> was typically 5–8 °C below the transition temperature T<sub>0</sub> for each sample.

Figure 5a illustrates X-ray reflectivity normalized to the Fresnel reflectivity, R/R<sub>F</sub>, from interfaces between 10<sup>−4</sup> M DHDP in dodecane and 10<sup>−5</sup> M SrCl<sub>2</sub> in water for all values of pH studied. The Fresnel reflectivity R<sub>F</sub> is calculated for a theoretical dodecane–water interface whose electron density varies as a step-function at the interface. Reflectivity curves for all values of pH exhibit similar shapes that are characteristic of a monolayer of DHDP, though the pH has a marked effect on the reflectivity data. The positions of the maxima and minima shift to lower Q<sub>z</sub> and the second oscillation at higher Q<sub>z</sub> is damped with successively higher pH. These features are primarily the result of increased interfacial roughness that is due to the reduced interfacial tension at higher pH. Larger roughness σ reduces the reflectivity intensity by a factor of ~exp[−Q<sub>z</sub><sup>2</sup>σ<sup>2</sup>].<sup>22,45</sup> The intensity of the low Q<sub>z</sub> peak varies nonmonotonically, first increasing, then decreasing with pH. As discussed in more detail later, this behavior shows that the interfacial excess of Sr<sup>2+</sup> increases with pH, which counteracts

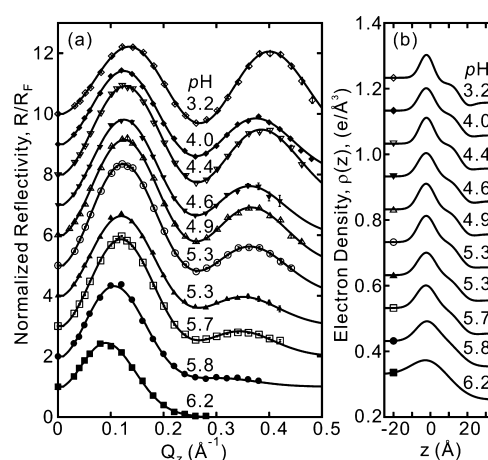


**Figure 5.** (a) X-ray reflectivity normalized to the Fresnel reflectivity, R/R<sub>F</sub>, from interfaces between 10<sup>−4</sup> M DHDP in dodecane and 10<sup>−5</sup> M SrCl<sub>2</sub> in water with pH indicated. Solid lines are the fits described in the text. Curves have been offset for clarity with the pH 6.2 sample plotted on an absolute scale (note that R/R<sub>F</sub> approaches 1 as Q<sub>z</sub> approaches 0 for all curves). Points at Q<sub>z</sub> = 0 are measured from transmission through the bulk organic phase. Solid and open symbols represent data taken at 9-ID and 15-ID, respectively. (b) Electron density profiles determined by the best fits shown in panel (a). The zero of the z-axis, z = 0, is arbitrarily located at the boundary between slabs 1 and 2. Curves have been offset for clarity with the pH 6.2 sample plotted on an absolute scale.

the reduction in intensity from increased roughness. Because the Sr<sup>2+</sup> excess saturates at some value of pH, the subsequent increase in roughness at even higher pH leads to a reduction in intensity of the low Q<sub>z</sub> peak.

**Fitting Reflectivity Data.** X-ray reflectivity data were fit initially by a monolayer model consisting of two slabs (N = 3 in eq 1), which represent the head and tail groups of DHDP. This model produced good fits, but with clearly observable residuals at large Q<sub>z</sub> (>0.35 Å<sup>−1</sup>). The quality of fit was improved significantly by adding a third slab to represent the terminal end

Table 2. Best-Fit Parameters to the Model in Eq 1 of the Reflectivity Data in Figure 5a<sup>a</sup>

pH	$\sigma$ (Å)	$d_1$ (Å)	$\rho_1$ ( $e^- \text{Å}^{-3}$ )	$d_2$ (Å)	$\rho_2$ ( $e^- \text{Å}^{-3}$ )	$d_3$ (Å)	$\rho_3$ ( $e^- \text{Å}^{-3}$ )	$A_D$ (Å <sup>2</sup> )	$A_{Sr}^{ref}$ (Å <sup>2</sup> )	$A_{Sr}^{\dagger}$ (Å <sup>2</sup> )
3.2 <sup>b</sup>	3.5 <sup>+0.2</sup> <sub>-0.2</sub>	3.8 <sup>+1.7</sup> <sub>-1.3</sub>	0.51 <sup>+0.1</sup> <sub>-0.06</sub>	16.8 <sup>+1.3</sup> <sub>-0.9</sub>	0.316 <sup>+0.002</sup> <sub>-0.003</sub>	3.8 <sup>+0.0</sup> <sub>-1.4</sub>	0.214 <sup>+0.002</sup> <sub>-0.034</sub>	42.1 <sup>+2.0</sup> <sub>-1.5</sub>	1036 <sup>+∞</sup> <sub>-650</sub>	N/A
4.0 <sup>c</sup>	4.2 <sup>+0.2</sup> <sub>-0.2</sub>	4.3 <sup>+1.2</sup> <sub>-1.8</sub>	0.51 <sup>+0.13</sup> <sub>-0.04</sub>	17.5 <sup>+1.0</sup> <sub>-0.4</sub>	0.324 <sup>+0.002</sup> <sub>-0.002</sub>	2.1 <sup>+1.5</sup> <sub>-0.2</sub>	0.180 <sup>+0.048</sup> <sub>-0.000</sub>	42.6 <sup>+1.7</sup> <sub>-1.4</sub>	300 <sup>+400</sup> <sub>-100</sub>	250 <sup>+20</sup> <sub>-20</sub>
4.4 <sup>b</sup>	3.8 <sup>+0.2</sup> <sub>-0.2</sub>	4.3 <sup>+1.2</sup> <sub>-1.8</sub>	0.52 <sup>+0.13</sup> <sub>-0.04</sub>	16.7 <sup>+1.4</sup> <sub>-0.9</sub>	0.330 <sup>+0.002</sup> <sub>-0.003</sub>	2.9 <sup>+0.9</sup> <sub>-1.2</sub>	0.214 <sup>+0.019</sup> <sub>-0.034</sub>	41.9 <sup>+3.2</sup> <sub>-1.3</sub>	250 <sup>+140</sup> <sub>-90</sub>	230 <sup>+30</sup> <sub>-20</sub>
4.6 <sup>c</sup>	4.4 <sup>+0.1</sup> <sub>-0.2</sub>	4.3 <sup>+1.2</sup> <sub>-1.8</sub>	0.53 <sup>+0.15</sup> <sub>-0.04</sub>	17.6 <sup>+1.2</sup> <sub>-0.7</sub>	0.324 <sup>+0.002</sup> <sub>-0.003</sub>	3.0 <sup>+0.8</sup> <sub>-0.7</sub>	0.196 <sup>+0.024</sup> <sub>-0.016</sub>	41.0 <sup>+2.0</sup> <sub>-1.7</sub>	190 <sup>+100</sup> <sub>-50</sub>	129 <sup>+13</sup> <sub>-14</sub>
4.9 <sup>b</sup>	4.2 <sup>+0.2</sup> <sub>-0.1</sub>	4.5 <sup>+1.0</sup> <sub>-2.0</sub>	0.53 <sup>+0.16</sup> <sub>-0.03</sub>	17.0 <sup>+1.6</sup> <sub>-0.7</sub>	0.328 <sup>+0.002</sup> <sub>-0.004</sub>	3.8 <sup>+0.0</sup> <sub>-1.7</sub>	0.218 <sup>+0.004</sup> <sub>-0.038</sub>	40.3 <sup>+2.9</sup> <sub>-2.1</sub>	170 <sup>+40</sup> <sub>-40</sub>	107 <sup>+12</sup> <sub>-9</sub>
5.3 <sup>b</sup>	4.3 <sup>+0.2</sup> <sub>-0.1</sub>	4.6 <sup>+0.9</sup> <sub>-2.1</sub>	0.53 <sup>+0.17</sup> <sub>-0.03</sub>	16.6 <sup>+1.5</sup> <sub>-0.5</sub>	0.333 <sup>+0.002</sup> <sub>-0.001</sub>	2.9 <sup>+0.9</sup> <sub>-1.2</sub>	0.218 <sup>+0.016</sup> <sub>-0.038</sub>	41.7 <sup>+2.8</sup> <sub>-1.4</sub>	130 <sup>+40</sup> <sub>-30</sub>	90 <sup>+9</sup> <sub>-9</sub>
5.3 <sup>c</sup>	4.8 <sup>+0.2</sup> <sub>-0.3</sub>	4.2 <sup>+1.3</sup> <sub>-1.7</sub>	0.54 <sup>+0.15</sup> <sub>-0.05</sub>	16.8 <sup>+1.5</sup> <sub>-0.9</sub>	0.326 <sup>+0.004</sup> <sub>-0.005</sub>	3.8 <sup>+0.0</sup> <sub>-2.1</sub>	0.225 <sup>+0.007</sup> <sub>-0.045</sub>	40.7 <sup>+2.6</sup> <sub>-1.4</sub>	180 <sup>+90</sup> <sub>-70</sub>	85 <sup>+8</sup> <sub>-8</sub>
5.7 <sup>b</sup>	5.0 <sup>+0.2</sup> <sub>-0.2</sub>	4.6 <sup>+0.9</sup> <sub>-2.1</sub>	0.53 <sup>+0.17</sup> <sub>-0.04</sub>	17.0 <sup>+1.3</sup> <sub>-0.6</sub>	0.327 <sup>+0.004</sup> <sub>-0.004</sub>	3.8 <sup>+0.0</sup> <sub>-1.5</sub>	0.215 <sup>+0.009</sup> <sub>-0.035</sub>	40.6 <sup>+1.6</sup> <sub>-1.9</sub>	140 <sup>+40</sup> <sub>-40</sub>	86 <sup>+9</sup> <sub>-8</sub>
5.8 <sup>c</sup>	5.8 <sup>+0.6</sup> <sub>-0.4</sub>	4.1 <sup>+1.4</sup> <sub>-1.6</sub>	0.54 <sup>+0.18</sup> <sub>-0.06</sub>	15.2 <sup>+3.3</sup> <sub>-1.7</sub>	0.336 <sup>+0.004</sup> <sub>-0.017</sub>	2.7 <sup>+1.1</sup> <sub>-1.7</sub>	0.273 <sup>+0.027</sup> <sub>-0.093</sub>	44.2 <sup>+1.8</sup> <sub>-3.8</sub>	140 <sup>+80</sup> <sub>-60</sub>	100 <sup>+9</sup> <sub>-9</sub>
6.2 <sup>c</sup>	8.3 <sup>+0.8</sup> <sub>-0.8</sub>	4.2 <sup>+1.3</sup> <sub>-1.7</sub>	0.54 <sup>+0.19</sup> <sub>-0.07</sub>	14.3 <sup>+2.5</sup> <sub>-1.3</sub>	0.333 <sup>+0.007</sup> <sub>-0.033</sub>	2.6 <sup>+1.2</sup> <sub>-1.6</sub>	0.239 <sup>+0.061</sup> <sub>-0.059</sub>	47.9 <sup>+0.2</sup> <sub>-2.9</sub>	105 <sup>+90</sup> <sub>-40</sub>	74 <sup>+6</sup> <sub>-7</sub>

<sup>a</sup>Subscripts 1, 2, and 3 represent, respectively, the head group, most of the tail group, and the disordered region at the terminal end of the tail group (that includes the methyl group) in contact with dodecane. Constraints on the parameters, including  $d_1 \in [2.5:5.5]$  Å,  $d_3 \in [1:3.8]$  Å, and  $\rho_3 \in [0.18:0.3]$   $e^- \text{Å}^{-3}$ , were used to reduce the computational time required for fitting. Additional constraints,  $d_2 \in [13:21]$  Å and  $\rho_2 \in [0.3:0.34]$   $e^- \text{Å}^{-3}$ , were required for the two highest pH samples due to the limited range of  $Q_z$ . Only the constraint on  $d_3$  influenced the best-fit values, but this constraint was necessary to produce physically sensible parameters for the third slab. The molecular area of DHDP,  $A_D$ , and the interfacial area per  $\text{Sr}^{2+}$  ion,  $A_{Sr}^{ref}$ , are calculated from eqs 7 and 10, respectively. The interfacial area per  $\text{Sr}^{2+}$  ion,  $A_{Sr}^{\dagger}$ , is determined by analysis of X-ray fluorescence data. <sup>b</sup>Measured at 15-ID. <sup>c</sup>Measured at 9-ID.

of the tail group chains in contact with the oil phase. Table 2 lists the best-fit parameters used to generate the solid lines in Figure 5a and the electron density profiles in Figure 5b. The fitted values of the interfacial roughness are slightly smaller than the calculated ones by  $\sim 0.5$ – $1$  Å, though this can be due to an interfacial bending rigidity of the monolayer on the order of  $20 k_B T$  or less (Table 1).<sup>22</sup>

**Head Group Region.** Correlations between the head group thickness and electron density fitting parameters  $d_1$  and  $\rho_1$  produced large standard deviations in these parameters. Nevertheless, the excess number of electrons per area in the head group region,  $d_1 \times (\rho_1 - \rho_0)$ , which is directly related to the number of  $\text{Sr}^{2+}$  ions in this region, has a small uncertainty. The excess number of head group electrons rises from a value of  $0.682^{+0.017}_{-0.013}$   $e^- \text{Å}^{-2}$  at pH 3.2 to a value of  $0.903^{+0.016}_{-0.010}$   $e^- \text{Å}^{-2}$  at pH 5.3, which suggests a steady increase with pH of the fraction of DHDP head groups bound to  $\text{Sr}^{2+}$  ions, ultimately saturating near pH 5.3. This is consistent with the variation in the intensity of the low  $Q_z$  peak in reflectivity, as previously described.

**Tail Group Region.** In spite of the substantial effect of pH on the head group slab, the tail group alkyl chains show little dependence on pH, except possibly at the two highest values of pH where the larger interfacial roughness limits the  $Q_z$  range of reflectivity measurements, indeed, eliminating the second peak (Figure 5a) and producing large uncertainties in the fitting (Table 2). The electron density  $\rho_2$ , which represents most of the chain, varies between 0.316 and 0.336  $e^- \text{Å}^{-3}$ , demonstrating that the chains are close-packed and all-trans over most of their length.<sup>46</sup> The lower electron density  $\rho_3$  of the third slab, which represents the end of the chain in contact with dodecane, suggests that the ends of the tail groups are disordered, e.g., with gauche conformations, or that there is a density depletion due to the lower electron density of the methyl end group in comparison to methylene groups along the chain.<sup>47</sup> Similar observations of long-chain alcohols at the hexane–water interface have been reported.<sup>15</sup> The small thickness ( $\sim 3$  Å) of slab 3 suggests that the chain disorder or density depletion exists only in 1–2 carbons at the end of the hydrocarbon chain. If this effect is attributed to chain disorder, then the influence of the disorder on the overall thickness is small. The total chain length, given by the sum  $d_2 +$

$d_3$  of the thickness of slabs 2 and 3, is within one standard deviation of the length of an all-trans alkyl chains, given by  $L_{trans} = 15 \times 1.27 \text{ Å (C–C)} + 1.5 \text{ Å (C–H)} = 20.6 \text{ Å}$ , except at the highest pH values of 5.6 and 6.2.<sup>46</sup> This indicates that the chains are oriented normal to the interface, except at the two highest pH values where the chains may be tilted.

**Interfacial Area per DHDP.** The area per DHDP molecule can be determined from the number of electrons per area in the slabs that constitute the monolayer by assuming which atoms correspond to which slab. Here, we assume that the separation between the head group slab 1, and the tail group slab 2 occurs at the center of the two C–O bonds and that dodecane molecules do not intercalate into the monolayer. Therefore, the area per DHDP molecule  $A_D$  can be calculated using the tail group parameters by

$$A_D = \frac{258}{d_2 \rho_2 + d_3 \rho_3} \quad (7)$$

where 258 is the total number of electrons in the two alkyl chains ( $2 \times [\text{CH}_3(\text{CH}_2)_{15}]$ ) in a DHDP molecule. Substituting best-fit parameters of slab 2 and 3 into eq 7 yields the molecular area  $A_D$  listed in Table 2. The molecular area varies from 40.3 to 42.6 Å<sup>2</sup>, except for the two highest values of pH. These values of  $A_D$  are just slightly larger than twice the cross-sectional area of a single all-trans alkyl chain ( $A_0 = 19.83 \text{ Å}^2$ ), determined by X-ray grazing incidence diffraction from a close-packed DHDP monolayer at the water–vapor interface.<sup>31</sup> Because the chains are nearly perpendicular to the interface, small variations in molecular area could be attributed to additional space between chains. This additional space per DHDP, estimated by  $L_{trans} \times (A_D - 2A_0)$ , can accommodate one dodecane molecule for every 10–14 DHDP molecules, which is calculated by considering that a dodecane molecule in a rotator phase occupies a volume of  $\sim 375 \text{ Å}^3$ .<sup>46</sup> If this would be taken into account in eq 7, then the numerator would be increased from 258 to 265 or 268 to account for the addition of 7–10 dodecane electrons per DHDP. This would raise the molecular area by a small amount,  $\sim 4\%$ , consistent with the original assumption that dodecane intercalation into the monolayer can be ignored when  $A_D$  is calculated.

**Interfacial Area per  $\text{Sr}^{2+}$  from Reflectivity Data.** Table 2 lists the interfacial area per  $\text{Sr}^{2+}$  ion,  $A_{Sr}^{ref}$ , determined from X-ray



reflectivity data. Although a more accurate measurement of the area per  $\text{Sr}^{2+}$  ion from X-ray fluorescence,  $A_{\text{Sr}}^{\text{fl}}$  will be described later, we present a method to determine  $A_{\text{Sr}}^{\text{ref}}$  that considers the possible components of the head group and appropriate constraints on their volume. The electron density  $\rho_1$  in the head group is due to a combination of water molecules,  $\text{Sr}^{2+}$  ions, phosphate head group ( $\text{PO}_4$ ) of DHDP, which may be protonated at lower pH (see Chart 1). Assuming that there is no unoccupied volume in slab 1, the total number of electrons in slab 1 is given by

$$\rho_1 d_1 A_D = N_{\text{Sr}} Z_{\text{Sr}} + N_{\text{H}_2\text{O}} Z_{\text{H}_2\text{O}} + N_{\text{PO}_4} Z_{\text{PO}_4} \quad (8)$$

and the volume of slab 1 is

$$d_1 A_D = N_{\text{Sr}} V_{\text{Sr}} + N_{\text{H}_2\text{O}} V_{\text{H}_2\text{O}} + N_{\text{PO}_4} V_{\text{PO}_4} \quad (9)$$

where  $N_j$  is the number of each species per DHDP molecule in slab 1 ( $N_{\text{PO}_4} = 1$ ). The number of electrons and volume of each species, respectively, is given by  $Z_j$  and  $V_j$ , where  $Z_{\text{H}_2\text{O}} = 10$ ,  $V_{\text{H}_2\text{O}} = 30 \text{ \AA}^3$ ,  $Z_{\text{Sr}} = 36$ ,  $V_{\text{Sr}} = 8.18 \text{ \AA}^3$  (calculated from X-ray diffraction<sup>48</sup>), and  $Z_{\text{PO}_4} = 48$ . The volume of the head group  $V_{\text{PO}_4} = 62_{-4}^{+4} \text{ \AA}^3$  is calculated from the reflectivity of the  $10^{-4} \text{ M}$  DHDP/pure water interface,<sup>9</sup> consistent with the value at the water–vapor interface ( $60 \text{ \AA}^3$ ).<sup>31</sup> Equations 8 and 9 contain two unknowns,  $N_{\text{Sr}}$  and  $N_{\text{H}_2\text{O}}$ . Solving for  $N_{\text{Sr}}$ , though keeping  $V_{\text{PO}_4}$  explicit for now, yields the interfacial area per  $\text{Sr}^{2+}$ , given by

$$A_{\text{Sr}}^{\text{ref}} = \frac{A_D}{N_{\text{Sr}}} = \frac{99.82 A_D}{(3\rho_1 - 1)d_1 A_D - 144 + V_{\text{PO}_4}} \quad (10)$$

Using the values of  $\rho_1$  and  $d_1$  listed in Table 2, the interfacial area per  $\text{Sr}^{2+}$  decreases from  $\sim 1000 \text{ \AA}^2$  at pH 3.2 to reach a saturation value of  $\sim 150 \text{ \AA}^2$  at pH 5.3, though the uncertainties on these values are large. Uncertainties on  $A_{\text{Sr}}^{\text{ref}}$  are determined by uncertainties on  $V_{\text{PO}_4}$ ,  $\rho_1$ ,  $d_1$ , and  $A$ , as well as correlations between fitting parameters. The qualitative variation is consistent with the earlier discussion on the variation with pH of the low  $Q_z$  peak and the total number of electrons per area,  $d_1 \times \rho_1$ , in the head group slab.

**X-ray Fluorescence Near Total Reflection.** XFNTD data were measured immediately after the reflectivity measurements for every sample at each temperature. To extract the scale factor  $C$  described in the Experimental Section, XFNTD data were also measured from reference sample interfaces between pure dodecane and a  $\text{SrCl}_2$  aqueous solution, with salt concentrations of 0.05 and 0.1 M at beamlines 15-ID and 9-ID, respectively. Figure 6a shows representative fluorescence spectra from the 0.05 M  $\text{SrCl}_2$  reference sample for a value of  $Q_z = 0.016 \text{ \AA}^{-1}$  above the critical  $Q_c (=0.010 \text{ \AA}^{-1})$  for total reflection and for a value below  $Q_c$  at  $Q_z = 0.008 \text{ \AA}^{-1}$ . Both  $K\alpha$  and  $K\beta_1$  emission lines from the Sr K shell were identified. The  $K\alpha$  line consists of two indistinguishable emission lines,  $K\alpha_1$  and  $K\alpha_2$ , whose expected energy separation of 67 eV is smaller than the detector resolution (175 eV measured peak width at 14.148 keV).

The fluorescence exhibits a remarkable enhancement from below to above  $Q_c$ , primarily because the effective penetration depth in the aqueous phase increases dramatically from  $\tilde{\Lambda} = 15 \text{ nm}$  at  $Q_z = 0.008 \text{ \AA}^{-1}$  to  $\tilde{\Lambda} = 6 \text{ \mu m}$  at  $Q_z = 0.016 \text{ \AA}^{-1}$ . However, the ratio of the effective penetration depth below and above  $Q_c$  is substantially smaller than the ratio of their fluorescence

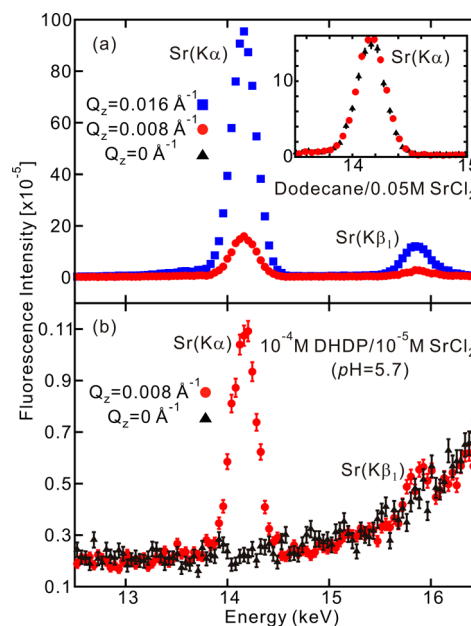


**Figure 6.** Normalized fluorescence spectra from two different samples at different values of  $Q_z$ . (a) The reference interface between pure dodecane and 0.05 M  $\text{SrCl}_2$  aqueous solution. The inset is an expanded view of the Sr  $K\alpha$  emission at  $Q_z = 0$  (background) and  $Q_z = 0.008 \text{ \AA}^{-1}$ . (b) The interface between  $10^{-4} \text{ M}$  DHDP in dodecane and  $10^{-5} \text{ M}$   $\text{SrCl}_2$  in water at pH = 5.7. Strontium  $K\alpha$  and  $K\beta_1$  emission lines are labeled. The increase in base intensity starting at  $\sim 15 \text{ keV}$  is the low energy tail of the Compton scattering peak located at  $\sim 19.3 \text{ keV}$  that is generated by the incident beam. The  $Q_z = 0$  background data are measured from a transmitted X-ray beam that passes through the dodecane phase within  $\sim 100 \text{ \mu m}$  of the interface, without reflecting off the interface.

intensities. The enhanced intensity below  $Q_c$  is due to the background intensity  $I_{\text{bg}}$ , whose measurement was described in the Experimental Section. The inset of Figure 6a demonstrates that the background dominates the low  $Q_z$  signal from the 0.05 M  $\text{SrCl}_2$  reference sample without DHDP.

Fluorescence spectra from the interface between  $10^{-4} \text{ M}$  DHDP in dodecane and  $10^{-5} \text{ M}$   $\text{SrCl}_2$  in water (pH 5.7) are shown in Figure 6b. The background signal at  $Q_z = 0 \text{ \AA}^{-1}$  does not show any sign of Sr fluorescence peaks, indicating that the background intensity  $I_{\text{bg}}$  vanishes for this low concentration  $\text{SrCl}_2$  solution. This also shows that the fluorescence intensity of  $\text{Sr}^{2+}$  ions extracted into the organic phase is below the detectable level. Therefore, the visible fluorescence signal at  $Q_z = 0.008 \text{ \AA}^{-1}$  (below  $Q_c$ ), where X-rays penetrate the interface evanescently for a short distance ( $\tilde{\Lambda} = 15 \text{ nm}$ ), is generated from only the interfacial region. The spectra in Figure 6b demonstrate that the concentration of  $\text{Sr}^{2+}$  ions is enhanced at the interface.

**Variation of Fluorescence with pH.** Figure 7 shows the integrated fluorescence intensity of the Sr  $K\alpha$  emission line as a function of wave vector transfer  $Q_z$ , measured from  $10^{-4} \text{ M}$  DHDP/ $10^{-5} \text{ M}$   $\text{SrCl}_2$  samples with pH values varying from 4.0 to 6.2. Samples with pH 3.2 did not produce enough fluorescence intensity to be analyzed. The results for the two reference samples are also presented. The integrated intensity is calculated from the product of the Sr  $K\alpha$  peak intensity and width obtained by fitting to a Gaussian function. The scale factor  $C$  is different at 15-ID and 9-ID, primarily as a result of the difference between absorber attenuation values used at the

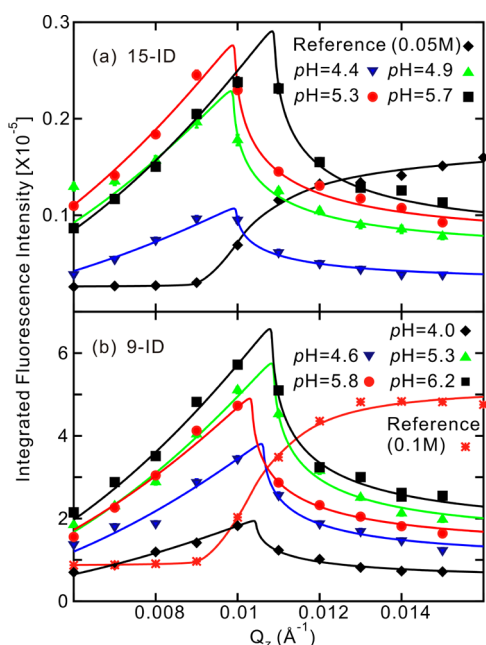


**Figure 7.** Integrated fluorescence intensity of Sr K $\alpha$  emission line as a function of  $Q_z$  from samples measured at beamlines (a) 15-ID and (b) 9-ID. The measured intensities from the reference samples are divided by a factor of 100. The concentration of the reference samples is 0.05 M in (a) and 0.1 M in (b). Solid lines are the best fits to eq 4.

two beamlines; therefore, the fluorescence data are displayed separately.

The  $Q_z$ -dependent fluorescence data from the two reference samples exhibit a sharp transition around the critical angle, similar to the behavior of the penetration depth of the incident beam into the aqueous phase. Assuming that the  $\text{Sr}^{2+}$  interfacial excess is negligible in the absence of DHDP in the organic phase, the data from the reference samples are fit to eq 4 without the interface term  $I_{\text{int}}$ . Best fits to the reference samples yield the scale factor  $C = (9.9 \pm 0.2) \times 10^{-7} \text{ Å}$  as well as the radius of interfacial curvature  $R_C = 194_{-19}^{+30} \text{ m}$  for the measurements at 15-ID, whereas  $C = (5.1 \pm 0.4) \times 10^{-8} \text{ Å}$  and  $R_C = 284_{-101}^{+360} \text{ m}$  for the measurements at 9-ID.

The fluorescence data from interfaces between  $10^{-4} \text{ M}$  DHDP in dodecane and  $10^{-5} \text{ M}$   $\text{SrCl}_2$  in water follow the shape of the Fresnel transmission coefficient  $T(\alpha')$ , which has a sharp peak at the critical angle (Figure 7). The shape of this feature is consistent with a signal that is dominated by the interfacial term in eq 4, as expected considering the small bulk concentration of the ion. Also, the sharpness of the peak indicates that these samples have negligible interfacial curvature. Although the critical  $Q_z$ , and therefore the position of the sharp peak, is expected to increase slightly with temperature, the variation of  $Q_c$  due to a small misalignment of the reflectometer for a given sample at fixed pH is substantially larger than the expected variation with temperature. The data, therefore, are fit to eq 4 without the background intensity  $I_{\text{bg}}$  or interfacial curvature, but with an additional fitting parameter that accounts for a small offset in  $Q_z$ , on the order of  $0.001 \text{ Å}^{-1}$  or less.

**Interfacial Area per  $\text{Sr}^{2+}$  from Fluorescence Data.** The best fits shown in Figure 7, combined with the scale factor  $C$  determined from the reference sample, yield the interfacial area per  $\text{Sr}^{2+}$  listed in the last column of Table 2 as  $A_{\text{Sr}}^{\text{fl}}$ . The interfacial area per  $\text{Sr}^{2+}$ ,  $A_{\text{Sr}}^{\text{fl}}$ , saturates near pH 5.3, consistent with the X-ray reflectivity results, though the values of  $A_{\text{Sr}}^{\text{fl}}$  are

smaller than those of  $A_{\text{Sr}}^{\text{ref}}$  and significantly more accurate. The higher accuracy of  $A_{\text{Sr}}^{\text{fl}}$  is a consequence of the element-specific nature of the fluorescence measurement and the limited range of  $Q_z$  in the reflectivity measurement. The saturation value ( $A_{\text{Sr}}^{\text{fl}} \sim 85 \text{ Å}^2$ ) suggests that there is one  $\text{Sr}^{2+}$  ion at the interface for every two DHDP head groups.

Figure 8 compares the interfacial coverage of  $\text{Sr}^{2+}$  ions, presented as the number of  $\text{Sr}^{2+}$  ions per  $100 \text{ Å}^2$  (essentially

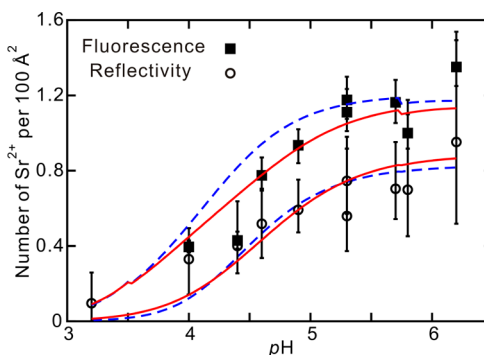


**Figure 8.** Variation with pH of the number of  $\text{Sr}^{2+}$  ions at the interface per  $100 \text{ Å}^2$ . Squares represent the result from fluorescence measurements and circles represent the result from reflectivity measurements. Lines are fits or calculations described in the Discussion. Red solid lines are determined from a model with 1:1 Sr:DHDP binding ( $K_{\text{Sr}1} = 0.25 \text{ M}^{-1}$ ;  $K_{\text{Sr}2} = 0$ ) and blue dashed lines from a model with 1:2 Sr:DHDP binding ( $K_{\text{Sr}1} = 0$ ;  $K_{\text{Sr}2} = 0.98 \text{ M}^{-1}$ ). The reflectivity data are fit with a Stern equation analysis. Additional  $\text{Sr}^{2+}$  ions in the diffuse electrical double layer are measured by the fluorescence. The interfacial density of these ions are calculated from a Gouy–Chapman model for the diffuse electrical double layer and added to the density determined by the fit to the reflectivity data to produce the lines that go through the fluorescence data. The small kink in the fits at  $\text{pH} \sim 5.75$  is the result of an abrupt change in monovalent ion concentration due to changing from an acetate buffer to a phosphate buffer (Table 1).

$A_{\text{Sr}}^{-1}$ ) from X-ray reflectivity and fluorescence measurements as a function of pH. Both sets of data exhibit the same trend, increasing from near zero at low pH and saturating near pH 5.3. The values from reflectivity measurements are systematically lower than those from the fluorescence measurements, due to the presence of  $\text{Sr}^{2+}$  in the diffuse part of the electrical double layer, as described in the Discussion.

**Temperature Dependence of the pH 5.3 Sample.** After measuring the pH 5.3 sample at  $37^\circ \text{C}$ , the sample was heated to  $50^\circ \text{C}$  and then cooled to  $38^\circ \text{C}$ . The sample was equilibrated, while stirring, for at least 2 h at each temperature before X-ray reflectivity and fluorescence data were measured. Figure 9 illustrates the results at these temperatures. The appearance of a change in reflectivity data over the temperature range from  $37$  to  $50^\circ \text{C}$  is in agreement with the phase transition temperature  $T_o = 44.1^\circ \text{C}$  measured with interfacial tension.

Far above  $T_o$  at  $50^\circ \text{C}$ , the reflectivity displays a single weak peak at a value of  $Q_z$  close to the position of the low- $Q_z$  peak observed below  $T_o$ . Analysis of the reflectivity using a two-slab model reveals an interface whose area per DHDP molecule has increased from the value of  $A_D = 40.7 \text{ Å}^2$  at  $37^\circ \text{C}$  to  $A_D = 83 \text{ Å}^2$  at  $50^\circ \text{C}$ , which illustrates a reduction in DHDP surface density by a factor of 2. The chains appear to be disordered, though the weak reflectivity leads to large uncertainties on the fitting parameters. Chain disordering alone cannot explain these

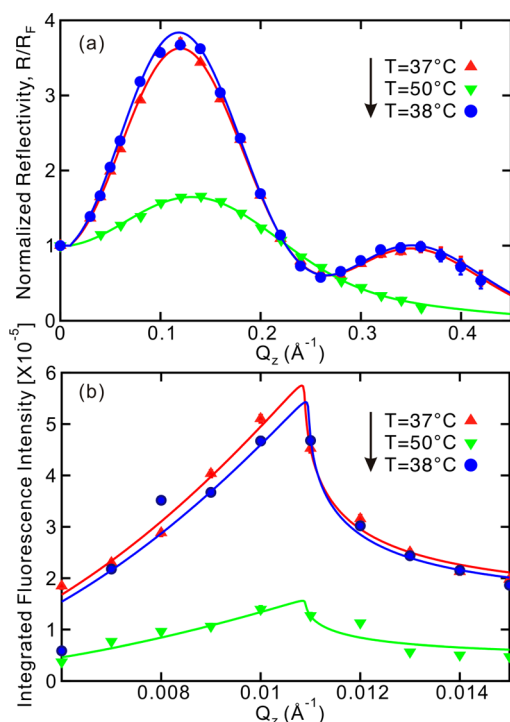


**Figure 9.** (a) Normalized reflectivity and (b) integrated fluorescence intensity of the sample with pH 5.3 at various experimental temperatures as labeled. The arrow indicates the temporal order of measurement.

data. The fluorescence indicates that the interfacial area per  $\text{Sr}^{2+}$  has increased from  $A_{\text{Sr}} = 85_{-8}^{+8} \text{ \AA}^2$  at  $37^\circ\text{C}$  ( $T < T_0$ ) to  $A_{\text{Sr}}^{\text{II}} = 315_{-44}^{+50} \text{ \AA}^2$  at  $50^\circ\text{C}$  ( $T > T_0$ ), a variation of  $\sim 3.5$ . Values of reflectivity and integrated fluorescence similar to those at  $37^\circ\text{C}$  are recovered upon cooling the sample below  $T_0$  to  $38^\circ\text{C}$  after being held at  $50^\circ\text{C}$  for  $\sim 7$  h (Figure 9). This shows that the interfacial structures are similar after heating and cooling through the transition. For example, the interfacial area of  $\text{Sr}^{2+}$  after cooling to  $38^\circ\text{C}$ ,  $A_{\text{Sr}}^{\text{II}} = 90_{-10}^{+16} \text{ \AA}^2$ , is indistinguishable from the original value of  $85_{-8}^{+8} \text{ \AA}^2$  at  $37^\circ\text{C}$ .

## DISCUSSION

**pH Dependence of Interfacial  $\text{Sr}^{2+}$ .** X-ray reflectivity and fluorescence results demonstrate a similar trend in  $\text{Sr}^{2+}$  binding with increasing pH, as shown in Figure 8. This trend can be understood as a competition between protons and strontium ions to bind with the DHDP phosphate head group. The Stern equation, which is a combination of the Langmuir adsorption isotherm and the conventional Poisson–Boltzmann description of the electrical double layer, can describe the competitive binding of  $\text{Sr}^{2+}$  ions.

**Stern Equation.** The relationship between the electric potential  $\phi(z)$  and the bulk ion number density  $n_j$  in the aqueous phase can be derived from the Poisson–Boltzmann equation in planar geometry (also known as the Gouy–Chapman equation),<sup>49,50</sup>

$$\frac{d^2\phi(z)}{dz^2} = \frac{-e}{\epsilon_0\epsilon_r} \sum_j Z_j n_j \exp[-Z_j e\phi(z)/k_B T] \quad (11)$$

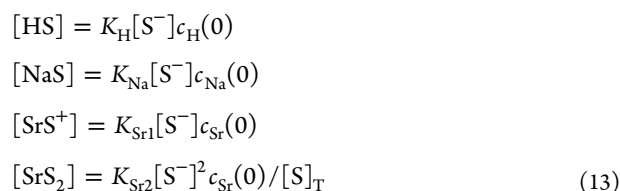
where  $e$  is the elementary charge,  $\epsilon_0$  is the vacuum permittivity,  $\epsilon_r$  is the relative permittivity,  $k_B$  is the Boltzmann constant, and  $n_j$  and  $Z_j$  represent the bulk number density and valence,

respectively, of the  $j$ th ion species in the bulk aqueous solution. An expression for the interfacial charge density  $\sigma_s$  (number of charges per unit area of the interface) is derived by integrating both sides of eq 11 with  $d\phi$  in the aqueous phase (with boundary conditions  $\phi(z \rightarrow \infty) = 0$  and  $(d\phi(z)/dz)_{z \rightarrow 0^+} = -\sigma_s/\epsilon_0\epsilon_r$ ),

$$\sigma_s = -\sqrt{2k_B T \epsilon_0 \epsilon_r} \left\{ \sum_j n_j (\exp[-Z_j e\phi(0)/k_B T] - 1) \right\}^{1/2} \quad (12)$$

a result known as the Grahame equation.<sup>51</sup>

Assuming that the Langmuir adsorption isotherm is applicable to our system, the binding reactions between the cations and the dissociated DHDP can be expressed as



where  $K_{\text{I}}$  is the binding constant (in units of  $\text{M}^{-1}$ ),  $[\text{IS}]$  is the surface density of ion-bound interface sites with  $\text{I}$  representing  $\text{H}^+$ ,  $\text{Na}^+$ , or  $\text{Sr}^{2+}$ ,  $[\text{S}^-]$  is the surface density of negative sites (i.e., dissociated DHDP),  $c_{\text{I}}(0) = c_{\text{I}} \exp[-Z_{\text{I}} e\phi(0)/k_B T]$  denotes the interfacial concentration in molarity of the cation  $\text{I}$ , and  $[\text{S}]_{\text{T}} = [\text{S}^-] + [\text{HS}] + [\text{NaS}] + [\text{SrS}^+] + 2[\text{SrS}_2] = 1/A_{\text{D}}$  is the total surface density of all sites. Although it may seem intuitive that divalent ions should bind to two DHDP<sup>−</sup> head groups, this issue has been debated for more than three decades in the related context of divalent ion binding to long-chain fatty acid Langmuir monolayers.<sup>33,52–55</sup> Diaz and coauthors have suggested that the propensity of divalent ions to bind to fatty acid head groups in Langmuir monolayers varies from ions such as  $\text{Ca}^{2+}$  and  $\text{Sr}^{2+}$ , which they predict to bind in a 1:1 stoichiometry, to ions such as  $\text{Pb}^{2+}$ , which they predict to bind preferably in a 1:2 stoichiometry.<sup>55,56</sup> Without loss of generality, both stoichiometries, i.e., 1:1 and 1:2 complexes of  $\text{Sr}^{2+}$  with a phosphate head group are considered here, as shown in eq 13.

The negative site binding with a monovalent or divalent ion with 1:2 stoichiometry will result in a neutral site, whereas binding of a divalent ion with 1:1 stoichiometry will produce a positive site. Therefore, the interface surface charge density is given by

$$\sigma_s = \left( \frac{-e}{A_{\text{D}}} \right) \Phi_{[\text{S}^-]} (1 - K_{\text{Sr1}} c_{\text{Sr}}(0)) \quad (14)$$

where  $\Phi_{[\text{S}^-]}$  is the fraction of dissociated DHDP,

$$\begin{aligned} \Phi_{[\text{S}^-]} &= [\text{S}^-]/[\text{S}]_{\text{T}} \\ &= (\sqrt{\Omega^2 + 8K_{\text{Sr2}}c_{\text{Sr}}(0)} - \Omega)/4K_{\text{Sr2}}c_{\text{Sr}}(0) \end{aligned} \quad (15)$$

with

$$\Omega = 1 + K_{\text{H}}c_{\text{H}}(0) + K_{\text{Na}}c_{\text{Na}}(0) + K_{\text{Sr1}}c_{\text{Sr}}(0) \quad (16)$$

The electric potential at the interface  $\phi(0)$  is determined self-consistently from eqs 12 and 14–16. Subsequently, eq 13 and the calculated value  $\phi(0)$  are used to express the interfacial area per bound  $\text{Sr}^{2+}$  as



$$A_{\text{Sr}} = \frac{A_{\text{D}}}{(K_{\text{Sr1}}\Phi_{[\text{S}^-]} + K_{\text{Sr2}}\Phi_{[\text{S}^-]^2})c_{\text{Sr}}(0)} \quad (17)$$

**Interfacial Density of  $\text{Sr}^{2+}$ .** Reflectivity and fluorescence results in Figure 8 exhibit a significantly different interfacial density of  $\text{Sr}^{2+}$  ions. In particular, XFNTNTR measures a larger density of  $\text{Sr}^{2+}$  ions (Figure 8). Although both techniques probe the bound ions just described in the previous paragraphs, the following discussion demonstrates that the reflectivity analysis is not sensitive to  $\text{Sr}^{2+}$  ions in the diffuse electrical double layer that extends into the aqueous phase for distances on the order of a Debye length, whereas the XFNTNTR technique records the fluorescence from these ions.

The analysis of X-ray reflectivity data assumed that a single slab could account for any additional electron density in the region of the DHDP head group, above that of the average constant value of the bulk aqueous phase. In other words, the variation in electron density due to an electrical diffuse double layer of ions was not taken into account explicitly in the analysis. Nevertheless, if these additional ions had a significant effect on the reflectivity, then we might expect that the fit would produce a head group thickness  $d_1$  ( $< 5 \text{ \AA}$ , Table 2) larger than the dimension of the phosphate group, which it does not. In addition, the high quality of the fits to the X-ray reflectivity data implies that the salient features of the electron density profile  $\rho(z)$  have been taken into account. As shown below, the  $\text{Sr}^{2+}$  ions in the diffuse double layer have an insignificant effect on the electron density in that region. Therefore, the interfacial density of  $\text{Sr}^{2+}$  determined by X-ray reflectivity measurements accounts for only  $\text{Sr}^{2+}$  ions bound to DHDP head groups, and not for free  $\text{Sr}^{2+}$  ions in the diffuse double layer.

XFNTNTR measurements, however, measure fluorescence from  $\text{Sr}^{2+}$  ions at distances from the interface determined by the penetration depth of the X-rays, whose smallest value of about 11 nm (at  $Q_z = 0.006 \text{ \AA}^{-1}$ ) is larger than the thickness of the region in our samples that contains  $\text{Sr}^{2+}$ . To account for  $\text{Sr}^{2+}$  in the diffuse double layer, we assume that the decay in electric potential  $\phi(z)$  is dominated by the 1:1 electrolytes (e.g.,  $\text{H}^+$  and  $\text{Cl}^-$ ;  $\text{Na}^+$  and  $\text{CH}_3\text{COO}^-$ ), whose concentration is typically 2 orders of magnitude larger than that of  $\text{Sr}^{2+}$  (Table 1). The electric potential and  $\text{Sr}^{2+}$  concentration in the diffuse layer are calculated using Gouy–Chapman theory to be<sup>57</sup>

$$\phi(z) = -\frac{2k_{\text{B}}T}{e} \ln\left(\frac{1 + \kappa e^{-z/\lambda_{\text{D}}}}{1 - \kappa e^{-z/\lambda_{\text{D}}}}\right) \quad (18a)$$

$$n_{\text{Sr}}(z) = n_{\text{Sr}} \left( \frac{1 + \kappa e^{-z/\lambda_{\text{D}}}}{1 - \kappa e^{-z/\lambda_{\text{D}}}} \right)^4 \quad (18b)$$

where  $\kappa = -\tanh(e\phi(0)/4k_{\text{B}}T)$  and  $\lambda_{\text{D}} = (\epsilon_0\epsilon_r k_{\text{B}}T/2e^2 n_{\text{mono}})^{1/2}$  is the Debye length (7–15 nm) with the total monovalent cation concentration given by  $n_{\text{mono}} = n_{\text{H}} + n_{\text{Na}}$ . Integration of eq 18b within  $\sim 1.5$  nm of the interface approximates the total  $\text{Sr}^{2+}$  in the diffuse layer due to the fast decay of  $n_{\text{Sr}}(z)$ .

Divalent ions usually bind more strongly than monovalent ions to phospholipids. For example, McLaughlin et al. measured the  $\zeta$  potential to obtain  $K_{\text{Sr}} = 14 \text{ M}^{-1}$  and  $K_{\text{Na}} = 0.6 \text{ M}^{-1}$  for phosphatidylserine.<sup>52</sup> This observation, combined with typical values of the electric potential at the interface ( $\phi(0) \approx -170$  to  $-130$  mV calculated from eqs 12 and 14), yields  $K_{\text{Sr1}}c_{\text{Sr}}(0) + 2K_{\text{Sr2}}c_{\text{Sr}}(0)\Phi_{[\text{S}^-]} \geq 10K_{\text{Na}}c_{\text{Na}}(0)$ . Thus,  $K_{\text{Na}} = 0$  is a good approximation to describe our data.

The reflectivity data in Figure 8 were fit to eqs 12, 14–16, and 17, using  $K_{\text{Na}} = 0$  and  $K_{\text{H}} = 100$ .<sup>58</sup> Ions from the buffer materials (e.g.,  $\text{Na}^+$  and  $\text{CH}_3\text{COO}^-$ ), whose concentrations are determined by the Henderson–Hasselbalch equation (Experimental Section), are taken into account in eq 12. Because samples at different pH's were also measured at different temperatures, the continuous fits represented by the lines in Figure 8 contain a smooth variation in temperature from one pH value to the next. This variation in temperature was constructed from the values in Table 1 by linear interpolation of the experimental temperature versus pH. Analysis of the reflectivity data indicates that the effects of  $K_{\text{Sr1}}$  and  $K_{\text{Sr2}}$  cannot be decoupled. We present two scenarios in Figure 8 that produce fits of nearly equivalent quality: 1:1 Sr:DHDP binding ( $K_{\text{Sr1}} = 0.25 \text{ M}^{-1}$ ;  $K_{\text{Sr2}} = 0$ ) and 1:2 Sr:DHDP binding ( $K_{\text{Sr1}} = 0$ ;  $K_{\text{Sr2}} = 0.98 \text{ M}^{-1}$ ).

Adding the  $\text{Sr}^{2+}$  ions calculated to be in the diffuse layer to those measured by X-ray reflectivity, as determined by the Stern equation analysis, generates the total  $\text{Sr}^{2+}$  interfacial densities shown in Figure 8 that pass through the fluorescence data. The model with 1:1 Sr:DHDP binding provides a better representation of the fluorescence data, though we cannot exclude the possibility of 1:2 Sr:DHDP binding or an interface with a mixture of 1:1 and 1:2 binding. Note that the presence of 1:1 Sr:DHDP binding does not violate charge neutrality as a result of the presence of other ions, such as unbound DHDP<sup>−</sup> ions or other ions in solution. Independent of the binding stoichiometry, the saturated value of  $A_{\text{Sr}}^{\text{II}} \sim 85 \text{ \AA}^2$  observed at higher pH (Table 2) suggests that there is one  $\text{Sr}^{2+}$  ion at the interface for every two DHDP molecules, as previously discussed in Results and Analysis.

#### Difficulty in Applying the Stern Equation to XFNTNTR Data.

The success of this analysis points out a shortcoming in applying the Stern equation directly to X-ray fluorescence near total reflection data. In this case, the Langmuir isotherm contained within the Stern equation would consider all  $\text{Sr}^{2+}$  ions measured by fluorescence to be bound to DHDP head groups. Because XFNTNTR data are sensitive to both bound and free (in the diffuse double layer)  $\text{Sr}^{2+}$  ions, the Stern equation would overestimate the binding constant (by a factor of 6, e.g., as determined by additional analysis for 1:1 binding). Nevertheless, the Stern equation proves adequate to describe X-ray reflectivity results, which are sensitive only to bound  $\text{Sr}^{2+}$  ions in our experiments. This is confirmed by noting that the excess free  $\text{Sr}^{2+}$  given by eq 18b increases the electron density of the diffuse layer over that of the bulk aqueous solution by only 2%, which is beyond the sensitivity of X-ray reflectivity. Although the determination of the binding constant by a fit to the ion interfacial density determined by X-ray reflectivity is simpler, because it involves only the Stern equation, the higher accuracy of the ion interfacial density determined by XFNTNTR justifies its measurement.

**Extraction of  $\text{Sr}^{2+}$ .** X-ray measurements show that heating a pH 5.3 sample from 37 °C ( $T < T_0$ ) to 50 °C ( $T > T_0$ ) reduces the interfacial concentration of DHDP by  $\sim 50\%$  and  $\text{Sr}^{2+}$  by  $\sim 70\%$  (as discussed in Results and Analysis). Interfacial Sr–DHDP complexes present at the interface below the transition could have been extracted into the organic phase or they might have dissociated into DHDP and  $\text{Sr}^{2+}$ , which subsequently dissolved into their preferred solvents (DHDP in dodecane and  $\text{Sr}^{2+}$  in water). Upon recooling below the transition, the interfacial structure remains the same as observed before heating above it. This implies that  $\text{Sr}^{2+}$  ions

are present in the aqueous solution even after keeping the sample above the transition temperature for many hours. Either  $\text{Sr}^{2+}$  ion extraction did not occur or  $\text{Sr}^{2+}$  is not fully extracted from the water.

Inductively coupled plasma atomic emission spectroscopy (ICP-AES) measured the aqueous phase Sr concentration of a pH 5.3 sample. An organic phase ( $10^{-4}$  M DHDP in dodecane) and aqueous phase ( $10^{-5}$  M  $\text{SrCl}_2$ ) of equal volume were placed in contact with each other in a glass dish at 50 °C for at least 7 h to mimic the experimental conditions for X-ray measurements. The results show that ~45% of  $\text{Sr}^{2+}$  ions are extracted with no time dependence beyond 7 h. Similar measurements on pH 3.2 and pH 6.2 samples showed that 5% and 55% of  $\text{Sr}^{2+}$  was extracted, respectively. The increase in extraction efficiency of  $\text{Sr}^{2+}$  with pH is consistent with earlier studies that used dibutyl phosphate as the extractant and chloroform as the organic solvent.<sup>59</sup> These measurements show that  $\text{Sr}^{2+}$  is only partially extracted from the water. Enough  $\text{Sr}^{2+}$  ions remain in the water after heating above the transition temperature and recooling to explain the reappearance of the interfacial  $\text{Sr}^{2+}$  observed by X-ray measurements.

**Comparison with  $\text{Er}^{3+}$  Extraction.** The present studies of  $\text{Sr}^{2+}$  extraction provide an interesting contrast with earlier studies of the extraction of  $\text{Er}^{3+}$  from  $\text{ErBr}_3$  and  $\text{ErCl}_3$  aqueous solutions into dodecane solutions of DHDP.<sup>9</sup> Similar protocols were used for both sets of studies, including those for sample preparation, interfacial tension, and X-ray measurements. The  $\text{Er}^{3+}$ –DHDP interfacial ion–extractant complex contained approximately three DHDP molecules (with an experimental upper limit of 3.8), which we refer to as  $\text{Er}(\text{DHDP})_3$ . Although there is some question as to the stoichiometry of the Sr–DHDP complex, either 1:1 or 1:2, this work has shown that interfaces saturated with  $\text{Sr}^{2+}$ , at higher pH, contain a total of one  $\text{Sr}^{2+}$  for every two DHDP molecules, which includes  $\text{Sr}^{2+}$  that is bound and in the diffuse double layer. We refer to this arrangement as a  $\text{Sr}(\text{DHDP})_2$  interfacial complex and illustrate it in Figure 10 as if the Sr is complexed to two DHDP

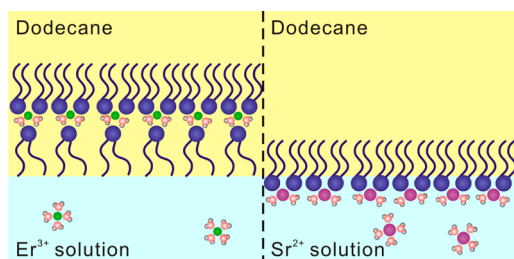


**Figure 10.** Cartoons of the interfacial structure observed in  $\text{Er}^{3+}$  (left) and  $\text{Sr}^{2+}$  (right) systems.

molecules. This arrangement allows for charge neutrality if each DHDP has one deprotonated phosphate, though it should be appreciated that complexing of these two metal ions with additional DHDP molecules is chemically plausible and has been observed in ion–extractant complexes in organic solution.<sup>5</sup>

The  $\text{Sr}(\text{DHDP})_2$  interfacial complex was observed as a result of the formation of a condensed interfacial monolayer of complexes below an adsorption transition. Likewise, the  $\text{Er}^{3+}$ –DHDP interfacial complex was observed as a result of the formation of a condensed interfacial inverted bilayer composed of the complexes illustrated in the left panel of Figure 10.<sup>9</sup> The

$\text{Sr}(\text{DHDP})_2$  interfacial complex conforms to common expectations of the behavior of amphiphiles at interfaces in which the polar head group of DHDP is exposed to the aqueous phase and DHDP tail groups extend into the region of dodecane. In contrast, the  $\text{Er}(\text{DHDP})_3$  interfacial complex was shown to take an unexpected form, in which polar DHDP head groups are separated from the aqueous phase and hydrophobic end groups are placed in contact with water. The formation of the inverted bilayer has been rationalized on the basis of the free energy gain from strong electrostatic interactions of the metal ions, as well as enhanced van der Waals interactions (per interfacial area) between alkyl chains, which dominate the energetic penalty of breaking hydrogen bonds between head groups and water.<sup>60,61</sup> The absence of an inverted bilayer at the interface in the  $\text{Sr}^{2+}$ –DHDP system may indicate that a +2 charge is inadequate to stabilize it or that it does not have a substantial energetic advantage over the monolayer geometry for complexing DHDP molecules to  $\text{Sr}^{2+}$ .

In the case of both  $\text{Er}^{3+}$  and  $\text{Sr}^{2+}$ , the condensed interfacial layer was formed by initiating extraction across the interface, then arresting or greatly retarding the extraction kinetics to immobilize the ion–extractant complexes at the interface. As described in detail elsewhere, the overall structure of the condensed interfacial layer containing  $\text{Er}^{3+}$  was sensitive to the thermal history of sample preparation.<sup>9</sup> Although the inverted bilayer was observed for a variety of thermal histories, different thermal protocols produced different types of inverted bilayers or, in some circumstances, inhomogeneous interfacial layers that appeared to consist of a mixture of monolayer and inverted bilayer. Such variability was not observed in the study of  $\text{Sr}^{2+}$ , which always produced the same monolayer structure of  $\text{Sr}(\text{DHDP})_2$  complexes. This may be attributable to the dynamical process that moves  $\text{Er}^{3+}$  ions out of the aqueous phase to form the inverted bilayer. It seems sensible to expect that arresting this dynamical process in different ways will lead to different final states of the immobilized interfacial condensed layer. A similar dynamical process does not seem to be necessary for the formation of the  $\text{Sr}(\text{DHDP})_2$  complexes, which leaves  $\text{Sr}^{2+}$  in the water, and may explain the consistent reproducibility of the  $\text{Sr}^{2+}$ –DHDP interfacial structure, both for the thermal protocol described earlier and for samples that were prepared with both aqueous and organic phases at a temperature below the transition.

Nevertheless, in the case of both  $\text{Er}^{3+}$  and  $\text{Sr}^{2+}$ , extraction requires removing the metal ion from the aqueous phase. Our study of the  $\text{Er}^{3+}$  system suggested a causal connection between the interfacial ion–extractant complexes and the extracted complexes observed by X-ray absorption spectroscopy in the organic solution. In this case the same 1:3 coordination ( $\text{Er}(\text{DHDP})_3$ ) was observed at the interface and in solution, though a minority component of higher aggregation number, to make an average of 4 DHDP to 1  $\text{Er}^{3+}$ , appeared to be present in solution. These observations are consistent with small angle neutron scattering (SANS) measurements that observed small, spherical extracted complexes of low aggregation number for a different trivalent ion,  $\text{Al}^{3+}$ .<sup>62</sup> In contrast, the  $\text{Sr}(\text{DHDP})_2$  complex measured at the interface contained  $\text{Sr}^{2+}$  ions located on the aqueous side of the interface. Therefore, a subsequent step in the extraction process must be responsible for transporting  $\text{Sr}^{2+}$  across the interface into the organic phase. It is unknown if this additional step in the extraction of  $\text{Sr}^{2+}$  is related to the lower extraction efficiency of ~50% as compared to the nearly complete extraction of  $\text{Er}^{3+}$  by DHDP at pH 2.5.

SANS measurements demonstrated that extracted complexes containing divalent metal ions ( $\text{Ca}^{2+}$ ,  $\text{Co}^{2+}$ ,  $\text{Ni}^{2+}$ ,  $\text{Cu}^{2+}$ , and  $\text{Mn}^{2+}$ ) often form cylindrical rod-shaped micelles that contain many more than 2 extractants.<sup>62</sup> It is unknown if these multicomplex reverse micelles are formed at the interface during a step that removes the divalent metal ion from the aqueous phase and how that extra step may be related to extraction efficiency.

## CONCLUSIONS

The efficiency of metal ion extraction is greatly influenced by pH and the valence of metal ions.<sup>59</sup> This study of  $\text{Sr}^{2+}$ , in combination with an earlier study of  $\text{Er}^{3+}$  ion extraction with the same DHDP extractant, provides insight into the different ion–extractant complexes that form at the interface in the midst of solvent extraction. X-ray reflectivity and X-ray fluorescence near total reflection (XFNTR) were used to characterize the ion–extractant interfacial complexes in both systems. An interfacial monolayer of DHDP extractants composed of one  $\text{Sr}^{2+}$  ion for every two DHDP molecules, which includes  $\text{Sr}^{2+}$  bound to DHDP and  $\text{Sr}^{2+}$  in the diffuse double layer, was observed for the  $\text{Sr}^{2+}$ –DHDP system at higher pH, in contrast to the inverted bilayer composed of one  $\text{Er}^{3+}$  for every three DHDP molecules observed for a similarly constituted  $\text{Er}^{3+}$ –DHDP system. The  $\text{Er}^{3+}$  in the interfacial ion–extractant complex are already removed from the aqueous phase, unlike the  $\text{Sr}^{2+}$  ions, which form a stable ion–extractant complex containing  $\text{Sr}^{2+}$  on the aqueous side of the interface. In the case of  $\text{Sr}^{2+}$ , a subsequent step in the extraction process is required to remove  $\text{Sr}^{2+}$  from the aqueous phase, which may be responsible for its lower extraction efficiency, in comparison to  $\text{Er}^{3+}$ , in this DHDP extractant system.

The role of pH on ion binding was also investigated. The monolayer structure of  $\text{Sr}^{2+}$  ion–extractant complexes was observed throughout the entire range of pH. The interfacial  $\text{Sr}^{2+}$  coverage below the transition temperature progressively increases from zero to saturation (one  $\text{Sr}^{2+}$  per two DHDP) within a narrow range of pH. On the basis of the sensitivity of scattering techniques, X-ray reflectivity detects  $\text{Sr}^{2+}$  primarily in the Stern layer of ions bound to DHDP phosphate head groups, whereas the fluorescence technique XFNTR probes both bound ions and those in the diffuse electrical double layer. The pH-dependent X-ray reflectivity results are described well by the Stern equation to yield the binding constant between DHDP and  $\text{Sr}^{2+}$ . Additional interfacial  $\text{Sr}^{2+}$  coverage observed by XFNTR measurements is in excellent agreement with an approximate Gouy–Chapman calculation without any fitting parameters, in which the electric potential in the diffuse layer is assumed to be dominated by the presence of monovalent electrolytes that are present at a much higher concentration.

## AUTHOR INFORMATION

### Corresponding Authors

\*W. Bu. E-mail: weibu@uic.edu.

\*L. Soderholm. E-mail: ls@anl.gov.

\*M. L. Schlossman. E-mail: schloss@uic.edu.

### Notes

The authors declare no competing financial interest.

## ACKNOWLEDGMENTS

This work was supported by the U.S. DOE, OBES, Chemical Sciences, Geosciences, and Biosciences Division under

Contract No. DE-AC02-06CH11357. The Advanced Photon Source (including Sector 9), OBES, Materials Sciences is supported under DE-AC02-06CH11357. M.L.S. also acknowledges support from NSF-CHE-0910825. ChemMatCARS (Sector 15 of the Advanced Photon Source) is supported by NSF-CHE-1346572.

## REFERENCES

- (1) Musikas, C.; Schulz, W. W. In *Principles and Practices of Solvent Extraction*; Rydberg, J., Choppin, M. C., Choppin, G. R., Eds.; Marcel Dekker: New York, 1992; pp 413–447.
- (2) Gupta, C. K.; Mukherjee, T. K. *Hydrometallurgy in Extraction Processes*; CRC Press: Boca Raton, FL, 1990.
- (3) Tasker, P. A.; Plieger, P. G.; West, L. C. Metal Complexes for Hydrometallurgy and Extraction. In *Comprehensive Coordination Chemistry II: From Biology to Nanotechnology*; McCleverty, J. A., Meyer, T. J., Eds.; Elsevier: Oxford, U.K., 2004; Vol. 9; pp 759–808.
- (4) *Ion Exchange and Solvent Extraction: A Series of Advances*; Moyer, B. A., Ed.; CRC Press: Boca Raton, FL, 2010; Vol. 19.
- (5) Gannaz, B.; Antonio, M. R.; Chiarizia, R.; Hill, C.; Cote, G. Structural Study of Trivalent Lanthanide and Actinide Complexes Formed Upon Solvent Extraction. *Dalton Trans.* **2006**, 38, 4553–4562.
- (6) Ellis, R. J.; Audras, M.; Antonio, M. R. Mesoscopic Aspects of Phase Transitions in a Solvent Extraction System. *Langmuir* **2012**, 28, 15498–15504.
- (7) Luo, G.; Bu, W.; Mihaylov, M.; Kuzmenko, I.; Schlossman, M. L.; Soderholm, L. X-Ray Reflectivity Reveals a Non-Monotonic Ion-Density Profile Perpendicular to the Surface of  $\text{ErCl}_3$  Aqueous Solutions. *J. Phys. Chem. C* **2013**, 117, 19082–19090.
- (8) Casillas-Ituarte, N. N.; Callahan, K. M.; Tang, C. Y.; Chen, X. K.; Roeselova, M.; Tobias, D. J.; Allen, H. C. Surface Organization of Aqueous  $\text{MgCl}_2$  and Application to Atmospheric Marine Aerosol Chemistry. *Proc. Natl. Acad. Sci. U. S. A.* **2010**, 107, 6616–6621.
- (9) Bu, W.; Yu, H.; Luo, G.; Bera, M. K.; Hou, B.; Lin, B.; Meron, M.; Kuzmenko, I.; Soderholm, L.; Antonio, M. Observation of a Rare Earth Ion-Extractant Complex Arrested at the Oil-Water Interface During Solvent Extraction. *J. Phys. Chem. B* **2014**, 118, 10662–10674.
- (10) Marcus, Y.; Kertes, A. S. *Ion Exchange and Solvent Extraction of Metal Complexes*; Wiley-Interscience: London, 1969.
- (11) Goebel, A.; Lunkenheimer, K. Interfacial Tension of the Water/N-Alkane Interface. *Langmuir* **1997**, 13, 369–372.
- (12) Zhou, N.-F.; Neuman, R. D. Dihexadecyl Phosphate Monolayers at the Heptane/Water Interface: Model Interfacial System for Solvent Extraction Studies. *Colloids Surf.* **1992**, 63, 201–207.
- (13) Pourbaix, M. *Atlas of Electrochemical Equilibria in Aqueous Solutions*; National Association of Corrosion: Houston, TX, 1974.
- (14) Adamson, A. W. *Physical Chemistry of Surfaces*, 5th ed.; John Wiley & Sons: New York, NY, 1990.
- (15) Tikhonov, A. M.; Pingali, S. V.; Schlossman, M. L. Molecular Ordering and Phase Transitions in Alkanol Monolayers at the Water-Hexane Interface. *J. Chem. Phys.* **2004**, 120, 11822–11838.
- (16) Pingali, S. V.; Takiue, T.; Luo, G.; Tikhonov, A. M.; Ikeda, N.; Aratono, M.; Schlossman, M. L. X-Ray Reflectivity and Interfacial Tension Study of the Structure and Phase Behavior of the Interface between Water and Mixed Surfactant Solutions of  $\text{CH}_3(\text{CH}_2)_{19}\text{OH}$  and  $\text{CF}_3(\text{CF}_2)_7(\text{CH}_2)_2\text{OH}$  in Hexane. *J. Phys. Chem. B* **2005**, 109, 1210–1225.
- (17) Julicher, F.; Lipowsky, R. Domain-Induced Budding of Vesicles. *Phys. Rev. Lett.* **1993**, 70, 2964–2967.
- (18) Zeppieri, S.; Rodriguez, J.; de Ramos, A. L. L. Interfacial Tension of Alkane Plus Water Systems. *J. Chem. Eng. Data* **2001**, 46, 1086–1088.
- (19) Mitrovanic, D. M.; Tikhonov, A. M.; Li, M.; Huang, Z.; Schlossman, M. L. Noncapillary-Wave Structure at the Water-Alkane Interface. *Phys. Rev. Lett.* **2000**, 85, 582–585.
- (20) Zhang, Z.; Mitrovanic, D. M.; Williams, S. M.; Huang, Z.; Schlossman, M. L. X-Ray Scattering from Monolayers of F-



(CF<sub>2</sub>)<sub>10</sub>(CH<sub>2</sub>)<sub>2</sub>OH at the Water-(Hexane Solution) and Water-Vapor Interfaces. *J. Chem. Phys.* **1999**, *110*, 7421–7432.

(21) Schlossman, M. L.; Synal, D.; Guan, Y.; Meron, M.; Shea-McCarthy, G.; Huang, Z.; Acero, A.; Williams, S. M.; Rice, S. A.; Viccaro, P. J. A Synchrotron X-Ray Liquid Surface Spectrometer. *Rev. Sci. Instrum.* **1997**, *68*, 4372–4384.

(22) Pershan, P. S.; Schlossman, M. L. *Liquid Surfaces and Interfaces: Synchrotron X-Ray Methods*; Cambridge University Press: Cambridge, U.K., 2012.

(23) Li, M.; Tikhonov, A.; Schlossman, M. L. An X-Ray Diffuse Scattering Study of Domains in F(CF<sub>2</sub>)<sub>10</sub>(CH<sub>2</sub>)<sub>2</sub>OH Monolayers at the Hexane-Water Interface. *Europhys. Lett.* **2002**, *58*, 80–86.

(24) Schlossman, M. L.; Tikhonov, A. M. Molecular Ordering and Phase Behavior of Surfactants at Water-Oil Interfaces as Probed by X-Ray Surface Scattering. *Annu. Rev. Phys. Chem.* **2008**, *59*, 153–177.

(25) Tamam, L.; Pontoni, D.; Sapir, Z.; Yefe, S.; Sloutskin, E.; Ocko, B. M.; Reichert, H.; Deutsch, M. Modification of Deeply Buried Hydrophobic Interfaces by Ionic Surfactants. *Proc. Natl. Acad. Sci. U. S. A.* **2011**, *108*, 5522–5525.

(26) Luo, G.; Malkova, S.; Yoon, J.; Schultz, D. G.; Lin, B.; Meron, M.; Benjamin, I.; Vanysek, P.; Schlossman, M. L. Ion Distributions near a Liquid-Liquid Interface. *Science* **2006**, *311*, 216–218.

(27) Luo, G.; Malkova, S.; Yoon, J.; Schultz, D. G.; Lin, B.; Meron, M.; Benjamin, I.; Vanysek, P.; Schlossman, M. L. Ion Distributions at the Nitrobenzene-Water Interface Electrified by a Common Ion. *J. Electroanal. Chem.* **2006**, *593*, 142–158.

(28) Elsen, A.; Festersen, S.; Runge, B.; Koops, C. T.; Ocko, B. M.; Deutsch, M.; Secek, O. H.; Murphy, B. M.; Magnussen, O. M. In Situ X-Ray Studies of Adlayer-Induced Crystal Nucleation at the Liquid-Liquid Interface. *Proc. Natl. Acad. Sci. U. S. A.* **2013**, *110*, 6663–6668.

(29) Elsen, A.; Murphy, B. M.; Ocko, B. M.; Tamam, L.; Deutsch, M.; Kuzmenko, I.; Magnussen, O. M. Surface Layering at the Mercury-Electrolyte Interface. *Phys. Rev. Lett.* **2010**, *104*, 105501.

(30) Laanait, N.; Mihaylov, M.; Hou, B.; Yu, H.; Vanysek, P.; Meron, M.; Lin, B.; Benjamin, I.; Schlossman, M. L. Tuning Ion Correlations at an Electrified Soft Interface. *Proc. Nat. Acad. Sci. U. S. A.* **2012**, *109*, 20326–20331.

(31) Bu, W.; Vaknin, D.; Travesset, A. How Accurate Is Poisson-Boltzmann Theory for Monovalent Ions near Highly Charged Interfaces? *Langmuir* **2006**, *22*, 5673–5681.

(32) Parratt, L. G. Surface Studies of Solids by Total Reflection of X-Rays. *Phys. Rev.* **1954**, *95*, 359–369.

(33) Bloch, J. M.; Yun, W. Condensation of Monovalent and Divalent Metal Ions on a Langmuir Monolayer. *Phys. Rev. A* **1990**, *41*, 844.

(34) Shapovalov, V. L.; Ryskin, M. E.; Konovalov, O. V.; Hermelink, A.; Brezesinski, G. Elemental Analysis within the Electrical Double Layer Using Total Reflection X-Ray Fluorescence Technique. *J. Phys. Chem. B* **2007**, *111*, 3927–3934.

(35) Bu, W.; Vaknin, D. X-Ray Fluorescence Spectroscopy from Ions at Charged Vapor/Water Interfaces. *J. Appl. Phys.* **2009**, *105*, 084911.

(36) Bu, W.; Flores, K.; Pleasants, J.; Vaknin, D. Preferential Affinity of Calcium Ions to Charged Phosphatidic Acid Surface from a Mixed Calcium/Barium Solution: X-Ray Reflectivity and Fluorescence Studies. *Langmuir* **2009**, *25*, 1068–1073.

(37) Vaknin, D.; Bu, W. Neutrally Charged Gas/Liquid Interface by a Catanionic Langmuir Monolayer. *J. Phys. Chem. Lett.* **2010**, *1*, 1936–1940.

(38) Bu, W.; Hou, B.; Mihaylov, M.; Kuzmenko, I.; Lin, B.; Meron, M.; Soderholm, L.; Luo, G.; Schlossman, M. L. X-Ray Fluorescence from a Model Liquid/Liquid Solvent Extraction System. *J. Appl. Phys.* **2011**, *110*, 102214.

(39) Henke, B. L.; Gullikson, E. M.; Davis, J. C. X-Ray Interactions: Photoabsorption, Scattering, Transmission, and Reflection at E=50–30000 Ev. *At. Data Nucl. Data Tables* **1993**, *54*, 181–342.

(40) Matubayasi, N.; Motomura, K.; Aratono, M.; Matuura, R. Thermodynamic Study on the Adsorption of 1-Octadecanol at Hexane/Water Interface. *Bull. Chem. Soc. Jpn.* **1978**, *51*, 2800.

(41) Takiue, T.; Uemura, A.; Ikeda, N.; Motomura, K.; Aratono, M. Thermodynamic Study on Phase Transition in Adsorbed Film of Fluoroalkanol at the Hexane/Water Interface. 3. Temperature Effect on the Adsorption of 1,1,2,2-Tetrahydroheptadecafluorodecanol. *J. Phys. Chem. B* **1998**, *102*, 3724.

(42) Berge, B.; Konovalov, O.; Lajzerowicz, J.; Renault, A.; Rieu, J. P.; Vallade, M.; Als-Nielsen, J.; Gruebel, G.; Legrand, J. F. Melting of Short 1-Alcohol Monolayers on Water: Thermodynamics and X-Ray Scattering Studies. *Phys. Rev. Lett.* **1994**, *73*, 1652.

(43) Gang, O.; Wu, X. Z.; Ocko, B. M.; Sirota, E. B.; Deutsch, M. Surface Freezing in Chain Molecules. II. Neat and Hydrated Alcohols. *Phys. Rev. E* **1998**, *58*, 6086.

(44) Sirota, E. B.; Wu, X. Z. The Rotator Phases of Neat and Hydrated 1-Alcohols. *J. Chem. Phys.* **1996**, *105*, 7763.

(45) Pershan, P. S. Structure of Surfaces and Interfaces As Studied Using Synchrotron Radiation: Liquid Surfaces. *Faraday Discuss. Chem. Soc.* **1990**, *89*, 231.

(46) Small, D. M. *The Physical Chemistry of Lipids*; Plenum: New York, NY, 1986.

(47) Ocko, B. M.; Dhinojwala, A.; Daillant, J. Comment on “How Water Meets a Hydrophobic Surface”. *Phys. Rev. Lett.* **2008**, *101*, 039601.

(48) Marcus, Y. Ionic Radii in Aqueous Solutions. *Chem. Rev.* **1988**, *88*, 1475–1498.

(49) Gouy, G. Constitution of the Electric Charge at the Surface of an Electrolyte. *J. Phys. (Paris)* **1910**, *9*, 457–467.

(50) Chapman, D. L. A Contribution to the Theory of Electrocapillarity. *Philos. Mag. Ser. 6* **1913**, *25*, 475–481.

(51) Grahame, D. C. The Electrical Double Layer and the Theory of Electrocapillarity. *Chem. Rev.* **1947**, *41*, 441–501.

(52) McLaughlin, S.; Mulrine, N.; Gresalfi, T.; Vaio, G.; McLaughlin, A. Adsorption of Divalent-Cations to Bilayer-Membranes Containing Phosphatidylserine. *J. General Physiology* **1981**, *77*, 445–473.

(53) Ahn, D. J.; Franes, E. I. Interactions of Charged Langmuir Monolayers with Dissolved Ions. *J. Chem. Phys.* **1991**, *95*, 8486–8493.

(54) Vollhardt, D.; Melzer, V. Phase Transition in Adsorption Layers at the Air-Water Interface: Bridging to Langmuir Monolayers. *J. Phys. Chem. B* **1997**, *101*, 3370.

(55) Diaz, M. E.; Cerro, R. L.; Montes, F. J.; Gala, M. A. Non-Ideal Adsorption of Divalent Cations on a Langmuir Monolayer: A Theoretical Model for Predicting the Composition of the Resulting Langmuir-Blodgett Films. *Chem. Eng. J.* **2007**, *131*, 155–162.

(56) Martin, M. E. D.; Montes, F. J.; Cerro, R. L. Surface Potentials and Ionization Equilibrium in Y-Type Deposition of Multiple Langmuir-Blodgett Films II. Theoretical Model. *J. Colloid Interface Sci.* **2005**, *185*, 694–702.

(57) Israelachvili, J. N. *Intermolecular and Surface Forces*; Academic Press: London, England, 1992.

(58) Tsukahara, S.; Yamada, Y.; Watarai, H. Effect of Surfactants on in-Plane and out-of-Plane Rotational Dynamics of Octadecylrhodamine B at Toluene-Water Interface. *Langmuir* **2000**, *16*, 6787–6794.

(59) Dyrssen, D.; Liem, D. H. Solvent Extraction Studies of Thorium(IV) by Dibutyl-Phosphate (DBP) in Chloroform, Hexol (Methylisobutylcarbinol) and Hexane. *Acta Chem. Scand.* **1964**, *18*, 224.

(60) Lorenz, C. D.; Travesset, A. Atomistic Simulations of Langmuir Monolayer Collapse. *Langmuir* **2006**, *22*, 10016–10024.

(61) Chevalier, N. R.; Chevallard, C.; Guenoun, P. Monovalent Cations Trigger Inverted Bilayer Formation of Surfactant Films. *Langmuir* **2010**, *26*, 15824–15829.

(62) Steytler, D. C.; Jenta, T. R.; Robinson, B. H.; Eastoe, J.; Heenan, R. K. Structure of Reversed Micelles Formed by Metal Salts of Bis(Ethylhexyl) Phosphoric Acid. *Langmuir* **1996**, *12*, 1483–1489.